https://doi.org/10.1070/RCR4967

Nonstoichiometry, structure and properties of nanocrystalline oxides, carbides and sulfides

Albina A.Valeeva,[a, b] Andrey A. Rempel,[a, b, c] Svetlana V. Rempel,[a, b] Stanislav I. Sadovnikov,[a] Aleksandr I. Gusev [a]

[a] *Institute of Solid State Chemistry, Ural Branch of the Russian Academy of Sciences, ul. Pervomayskaya 91, 620990 Ekaterinburg, Russian Federation*
[b] *Ural Federal University named after the first President of Russia B.N.Yeltsin, ul. Mira 19, 620002 Ekaterinburg, Russian Federation*
[c] *Institute of Metallurgy, Ural Branch of the Russian Academy of Sciences, ul. Amundsena 101, 620016 Ekaterinburg, Russian Federation*

The results of recent experimental studies of the influence of the size of oxide, carbide and sulfide nanoparticles on changes in their nonstoichiometry are analyzed and generalized. In relation to intrinsically nonstoichiometric titanium oxides and niobium and vanadium carbides, on the one hand, and stoichiometric silver sulfides, on the other hand, it is shown that a decrease in the particle size to the nano scale has a strong impact on the chemical composition of nanocrystalline compounds, *viz*., it leads to the occurrence of or increase in nonstoichiometry. A conclusion is drawn that interplay between the particle size and nonstoichiometry is common to all solid nanocrystalline substances and should be taken into account in studies on the synthesis, structure and properties of these systems.
The bibliography includes 260 references.

Contents

1. Introduction 601
2. Nanocrystalline nonstoichiometric titanium oxides 603
   2.1. Titanium monoxide 603
   2.2. Titanium dioxide 607
   2.3. Effect of nonstoichiometry and size of TiO_y nanoparticles on the structure and properties of hydroxyapatite-based nanocomposites 608
3. Nanocrystalline nonstoichiometric carbides 610
4. Nonstoichiometry of sulfides 613
   4.1. The structure and properties of nonstoichiometric nanoscale sulfides 613
   4.2. Nonstoichiometry of nanostructured silver sulfide 615
5. Note added in proof 619
6. Conclusion 621
7. List of acronyms 621

1. Introduction

The properties of chemical compounds are determined by their composition and structure, *i.e*., by the ratio of different-type atoms and by the mutual position of these atoms in space.

According to Proust's law of definite proportions,[1] a pure chemical compound has a fixed composition, which is independent of the method of preparation, being a chemical characteristic of the compound. Dalton's law of multiple proportions [2] states that for any compound the quantitative proportion of the constituent elements can be represented as the ratio of small integer numbers, *i.e*., the stoichiometric ratio. The notion 'stoichiometry' was introduced in the 1790s by J.B.Richter in his book '*Anfangsgründen der Stöchiometrie: oder, Messkunst chemischer Elementen*'.[3] For instance, the atomic ratio of hydrogen to sulfur in the hydrogen sulfide molecule is 2 : 1, the atomic ratios of nitrogen to oxygen in the nitrous oxide and nitrogen monoxide molecules are 2 : 1 and 1 : 1, respectively, *etc*. The conclusions drawn by Proust and Dalton were based on the results of studying a few oxide compounds including water, gases (swamp gas — methane, acetylene, hydrogen sulfide, *etc*.) and organic compounds. More recently, it was shown that the law of definite proportions and the law of multiple proportions are valid for molecular substances, in particular, gases and organic compounds. Indeed, a French chemist C.L.Bertholett,[4] who intensively studied metal alloys, arrived at the conclusion that there are a lot of solids of variable composition where the atomic ratio of constituent elements can change continuously; therefore, such compounds are nonstoichiometric. Nonstoichiometry is only possible in compounds containing two or more kinds of atoms.

Most binary and multicomponent inorganic solids are nonstoichiometric. Nonstoichiometry as fundamental structural-chemical characteristic of inorganic substances is first of all of interest to solid state chemistry [5] and many related disciplines from solid state physics to materials science. Researchers working in all areas of solid state science and in applied materials science (especially, semiconductor electronics) [6] utilize nonstoichiometry for controlling the properties of nonstoichiometric substances.

Nonstoichiometric solids include metal oxides, carbides, nitrides, borides, hydrides, sulfides and certain ternary

Received 5 June 2020
© 2021 Uspekhi Khimii, ZIOC RAS, Russian Academy of Sciences and IOP Publishing Limited

compounds. It follows that nonstoichiometry occurs widely in solid compounds.

Nonstoichiometry is related to structural defects in solids. A crystal, as a periodic 3D ordered ensemble of particles, is only a model of a perfect solid. Real crystals contain various defects and are characterized by larger or smaller deviations from stoichiometry.

Nonstoichiometry in solids is mainly associated with point defects such as structural vacancies. By structural vacancy is meant an unoccupied lattice site. The presence of structural vacancies causes changes in the atomic ratio, *i.e.*, in the stoichiometry of a crystal. This is a fundamental distinction between structural vacancies and the Frenkel, Schottky and anti-Schottky defects; the latter also belong to point defects but have no impact on the stoichiometry of crystals. Nonstoichiometry in binary compounds can also be due to the presence of antistructural defects (antisites), which appear when, *e.g.*, type-A atoms occupy sites in the sublattice formed by type-B atoms. Antistructural defects occur in alloys and substitutional solid solutions.

Thus, the main feature of nonstoichiometry in a certain compound is mismatch between the atomic ratio of constituent elements (*i.e.*, chemical composition) and the concentration of lattice sites occupied by the corresponding atoms. Nonstoichiometry can only occur in binary and multicomponent systems and, as an important scientific notion, it is described in quite detail in the Great Russian Encyclopedia.[7] The existence of real crystalline systems with defects means that the stoichiometric composition of a solid crystalline compound is more exception than rule.

There are many natural compounds with high concentration of vacancies under normal conditions. Among them, wüstite (FeO) is best known. Formally, this compound is oxygen-rich owing to high concentration of vacancies in the iron sublattice.[8] Wüstite is not available in the stoichiometric form since its homogeneity range varies from $Fe_{0.84}O$ to $Fe_{0.96}O$ and does not include the stoichiometric composition. Mismatch between the stoichiometric composition and the homogeneity range of a compound is characteristic of many solids. The authors of a study[9] on microwave-assisted synthesis of magnetite (Fe_3O_4) nanoparticles noted that an increase in their saturation magnetization can be due to the formation of nonstoichiometric iron oxide phases in the surface layer.

Large deviations from stoichiometry caused by the presence of structural vacancies in the metal sublattice are observed for hexagonal iron sulfide $Fe_{0.85}S$ with a *B*8-type (NiAs) structure[10] and for hexagonal and monoclinic copper disulfides whose composition varies from Cu_2S to $Cu_{1.96}S$, $Cu_{1.80}S$ and $Cu_{1.75}S$ according to different authors. Structural vacancies in the oxygen sublattice are responsible for large deviations from stoichiometry in many oxides including TiO_2, MnO_2, V_2O_5, Ta_2O_5, CeO_2, UO_2, MoO_3, WO_3, *etc.*

Intensive research into oxides, carbides, sulfides and selenides carried out in the first half of the 20th century revealed nonstoichiometric phases with very wide homogeneity ranges. For instance, the homogeneity range of cubic titanium monoxide spans from $TiO_{0.65-0.80}$ to $TiO_{1.25-1.33}$. Very high content of structural vacancies in the cubic and hexagonal oxide, sulfide, carbide and nitride phases stimulated a heated discussion about the character of vacancy distribution in the crystal lattice. In the 1960s – 2000s, a fraught debate of the problem of nonstoichiometry and ordering in oxides, carbides, sulfides and chalcogenides[11–16] was followed by introducing a concept which treats a vacant site (structural vacancy) as being a structural element of the crystal similar to an occupied site.

Research into nanocrystalline state of matter has been rapidly progressing since 1990.[17–20] More than 900 reviews on different aspects of the nanocrystalline state of chemical compounds are available. Among them, there is a short survey[21] of the use of different chemical elements in nanomaterials. Its authors noted that chemical features of each element manifest themselves more pronouncedly and clearly in the field of nanotechnology and thus to a great extent predetermine the application fields of nanomaterials. By varying the chemical diversity of the elements and by combining them properly (especially, oxygen compounds with metals and nonmetals) one can design different forms of nanostructured materials.

Studies of many nanoscale oxides, carbides, sulfides, chalcogenides and other compounds revealed nonstoichiometry that was not observed in coarse-crystalline

A.A.Valeeva. Candidate of Sciences (Chemistry), Associate Professor, Senior Researcher, Laboratory of Nonstoichiometric Compounds at ISSC, Ural Branch of the RAS, and Associate Professor at Ural Federal University.
E-mail: anibla_v@mail.ru
Current research interests: nonstoichiometry and ordering in oxides and oxide nanomaterials, structure and properties of nonstoichiometric oxides.
A.A.Rempel. Academician of the RAS, Professor, Doctor of Sciences (Physics and Mathematics); Director of the Institute of Metallurgy, Ural Branch of the Russian Academy of Sciences; Head of Laboratory of High-Entropy Alloys at IMET, Ural Branch of the RAS; Professor at Department of Physical Techniques and Devices for Quality Control, Institute of Physics and Technology, Ural Federal University.
E-mail: rempel.imet@mail.ru
Current research interests: nonstoichiometry, structural defects, disorder – order phase transitions, quantum size effects, nanomaterials, nanotechnologies.
S.V.Rempel. Candidate of Sciences (Physics and Mathematics), Associate Professor, Leading Researcher at Laboratory of Nonstoichiometric Compounds at ISSC, Ural Branch of the RAS, and Leading Researcher at Ural Federal University.
E-mail: svetlana_rempel@ihim.uran.ru
Current research interests: optical materials, luminescence, quantum dots, biolabels, biomaterials, nanostructured oxides and sulfides, nanocomposite materials.
S.I.Sadovnikov. Candidate of Sciences (Chemistry), Senior Researcher, Laboratory of Nonstoichiometric Compounds at ISSC, Ural Branch of the RAS.
E-mail: sadovnikov@ihim.uran.ru
Current research interests: synthesis, structure and reactivity of metal chalcogenides, colloidal solutions, nanoparticles, nanostructured materials.
A.I.Gusev. Doctor of Sciences (Physics and Mathematics), Professor, Principal Researcher, Laboratory of Nonstoichiometric Compounds at ISSC, Ural Branch of the RAS.
E-mail: gusev@ihim.uran.ru
Current research interests: nonstoichiometry and ordering in solids, thermodynamics, disorder – order phase transitions, nanocrystalline state of condensed matter.

Translation: A.M.Raevskiy

compounds but appeared with decreasing particle (grain, crystallite) size to the nano scale.[22–28] In some cases, combining the small particle size and nonstoichiometry is used as specific tool for controlling the properties of nanocrystalline nonstoichiometric compounds.

As far as we know, no summary reviews concerned with joint analysis of nonstoichiometry and small particle size of solid compounds have been reported as yet. In this review we tried to bridge the gap. To this end, we chose fundamentally different substances, *viz*., nonstoichiometric transition-metal compounds (niobium and vanadium carbides and titanium oxides) with high intrinsic nonstoichiometry and silver sulfides, which are traditionally treated as stoichiometric compounds. Well-studied titanium monoxide and titanium dioxide have never been considered from the standpoint of interplay between particle size and nonstoichiometry in both disordered and ordered phases. Niobium and vanadium carbides were chosen since these compounds are used as dopants for hard alloys. Noteworthy is that these carbides exist in hard alloys as nanoscale ordered phases. Coarse-crystalline lead and silver sulfides were considered as stoichiometric compounds for more than 100 years; however, they become nonstoichiometric on going to a nano state since sulfur atoms occupy new crystallographic positons in the cubic lattice of the former compound and due to the appearance of vacancies in the silver sublattice of the latter.

2. Nanocrystalline nonstoichiometric titanium oxides

The Ti–O system is one of the best studied and practically important binary transition metal–oxygen systems. There are at least 15 different titanium oxides including Ti_6O, Ti_3O, Ti_2O, TiO, Ti_2O_3, Ti_3O_5, Ti_nO_{2n-1} ($n = 4–10$) and TiO_2.[29,30] Most compounds belonging to this system are characterized by wide homogeneity ranges, thus being nonstoichiometric.[30] Nonstoichiometry in titanium oxides can exist either in one (usually, oxygen) or both (oxygen and titanium) sublattices.

2.1. Titanium monoxide

Cubic titanium monoxide TiO_y (space group $Fm\bar{3}m$) is characterized by the widest homogeneity range among all titanium oxides. The compound has a $B1$-type structure and exists in the composition range from $TiO_{0.70}$ to $TiO_{1.25}$. A unique feature of titanium monoxide $TiO_y = Ti_xO_z$ ($y = z/x$) is simultaneous presence of structural vacancies in both, titanium and oxygen, sublattices.[31–33] The concentration of vacancies in the monoxide $TiO_{1.00} = Ti_{0.833}O_{0.833}$ ranges from $\sim$10 at.% to $\geqslant$16 at.%. Structural vacancies as structural elements of titanium monoxide appear during the synthesis of the compound and stabilize it.

Finely dispersed (microcrystalline) titanium monoxide powders are prepared *in vacuo* by high-temperature synthesis from mixtures of powdered titanium dioxide and metallic titanium. Structural vacancies are responsible for the formation of different ordered phases of TiO_y and for the occurrence of concentration and temperature-induced order–disorder phase transitions. Titanium monoxide with ordered or disordered distribution of structural vacancies is prepared using additional vacuum annealing at different temperatures.

Data on the formation of different ordered phases (superstructures) of titanium monoxide are contradictory. It was reported[33–40] that the symmetry of superstructures changes from cubic and hexagonal to monoclinic. The formation of several ordered phases of the monoxide $TiO_{1.0}$ is possible. An equilibrium monoclinic superstructure $Ti_5\blacksquare O_5\square = Ti_{0.83}O_{0.83}$ ($\blacksquare$ and $\square$ are vacancies in the titanium and oxygen sublattice, respectively) exists in the temperature range of 1253–1263 K.[33,34] The formation of ordered cubic phase of stoichiometric monoxide $TiO_{1.0}$ at higher temperatures (1263–1523 K) was also reported.[34]

More recently,[35,36] a model was proposed for the cubic superstructure Ti_5O_5 ($Ti_5\blacksquare O_5\square \equiv Ti_{90}\blacksquare_{18}O_{90}\square_{18}$) of nonstoichiometric titanium monoxide; the lattice constant of this superstructure is three times larger than that of the basis disordered $B1$-type structure of titanium monoxide. The synthesis of a new polymorph of titanium monoxide, ε-TiO, was reported.[37] A single crystal of ε-TiO had a hexagonal structure (space group $P\bar{6}2m$). According to calculations,[37] ε-TiO is more stable than the ordered monoclinic phase. In addition, an orthorhombic (space group $I222$) superstructure with ordered arrangement of oxygen vacancies and randomly distributed vacancies in the titanium sublattice is formed in the composition range of $TiO_{0.7}–TiO_{0.9}$ at $T > 873$ K.[31] These data[31] contradict the results of studies[38,40] in which a monoclinic ordered phase (space group $C2/m$ or $A2/m$) was detected in titanium monoxide containing from 36 to 50 at.% of oxygen (in the composition range from $TiO_{0.56}$ to $TiO_{1.00}$) and annealed to low temperatures. An orthorhombic (space group $Immm$, $Imm2$ or $I222$) ordered phase $TiO_{1.20}$, stable at $\leqslant$1093 K, and a tetragonal (space group $I4/m$, $I4$ or $I\bar{4}$) superstructure $Ti_4O_5 = TiO_{1.25}$, stable at $T < 993$ K, were observed in superstoichiometric monoxides (composition range from $TiO_{1.00}$ to $TiO_{1.50}$) containing vacancies mainly in the metal sublattice.[34]

Recently, considerable attention has been paid to the dependence of nonstoichiometry, stability, properties and structural characteristics of titanium monoxide on the particle size. There are a number of studies on the size effects in titanium monoxide on going from micro- to nanocrystals.[26,41–43] Particles of nanocrystalline substances have a larger specific surface area and an excess free energy, which significantly changes their thermodynamic characteristics and properties. This offers great prospects for imparting different properties to nanomaterials (based on the same chemical elements) built of different-size structural blocks with different ordering patterns.

Nanocrystalline titanium monoxide can be prepared by mechanochemical treatment (dispersion) of powdered mixtures of titanium and titanium dioxide.[44–46] For instance, a titanium monoxide nanopowder was synthesized[44] from different powder mixtures:

— unmilled titanium mixed with unmilled TiO_2 (anatase),

— unmilled titanium mixed with 30-h milled anatase, and

— 30-h milled titanium with 30-h milled anatase.

In all experiments, the components were mixed in a 1 : 1 weight ratio. The mixtures were milled in a ball mill at 600 rpm and then annealed in nitrogen or argon atmosphere at 1170 K for 2 h. The particle size was 35–130 nm after annealing in argon and 48–110 nm after annealing in nitrogen. It was found that the powder morphology depends on the milling and annealing conditions.

Nanocrystalline monoxide TiO_y of different nonstoichiometry ($y = 0.92$, 0.99, 1.19) was prepared by mechano-

chemical synthesis from mixtures of Ti and TiO_2 (rutile) powders taken in 1 : 1, 1.10 : 1 and 1.25 : 1 molar ratios.[45] Milling in a planetary ball mill for 2 h in either air or argon atmosphere gave cubic TiO_y nanopowders with a particle size of 6 nm. It was shown that nonstoichiometry (phase composition) can be controlled by varying the initial $Ti : TiO_2$ powder ratio while the structure can be controlled by subsequent vacuum annealing at 1170 – 1270 K (depending on the composition, crystallization of the powder leads to formation of a monoclinic or cubic phase).

Titanium monoxide nanopowder was obtained[46] by low-energy wet ball milling of commercially available titanium monoxide powder in deionized water with Pluronic F127 additive. The suspension was milled in a TURBULA-T 2F shaker mixer with zirconia balls at 72 rpm for 72 h. According to X-ray diffraction data, the particle size was at most 8 nm after milling.

Specific features of the microstructure of finely dispersed cubic monoxide TiO_y powders influence the structure and properties of nanocrystalline TiO_y. In this connection, the microstructure of coarse-crystalline powders $TiO_{0.92}$, $TiO_{0.99}$, $TiO_{1.09}$ and $TiO_{1.26}$ (average particle size of ~25 μm) synthesized by vacuum solid-phase sintering of titanium and TiO_2 was studied[47] by X-ray diffraction, optical and electron microscopy. Samples of disordered TiO_y were prepared by vacuum annealing of the synthesized samples at 1330 K followed by quenching at a rate of 200 K s^{-1} to room temperature; ordered samples were obtained by vacuum annealing at 1330 K for 3 h followed by slow cooling to 300 K at a rate of 10 K h^{-1}. The disordered powders, $TiO_{0.92}$, $TiO_{0.99}$, $TiO_{1.09}$ and $TiO_{1.26}$, have a layered structure with steps. The layers mainly grew in one direction and the step size was fixed. Longitudinal and transverse chips observed on the surface of particles suggest the presence of mechanical twins, annealing twins and intermittent motion of twin boundaries. The step edges curved in different manner upon deviation of the titanium monoxide composition from the stoichiometric ratio to both $TiO_{0.92}$ and $TiO_{1.26}$ owing to different impact of vacancies present in both sublattices of the sub- and superstoichiometric titanium monoxides since the concentrations of vacancies are different.

Heat treatment (annealing or quenching) of the TiO_y samples led to the onset of local overstresses and to the appearance of dislocations. The motion and interaction of dislocations manifested itself on the surface of samples as triangular precipitates (deformation twin rosettes). The concentration of triangular precipitates in the disordered monoxide TiO_y was lower than in the ordered monoxide of the same composition; however, their shape and size were preserved. This type of the microstructure is due to the formation and growth of the ordered monoclinic phase domains inside the cubic matrix, which causes large microdeformations and cracking of samples along the grain boundaries. The microstructure of superstoichiometric monoxide $TiO_{1.26}$ has a peculiar feature, *viz*., inclusions of the trigonal (space group $R\bar{3}c$) Ti_2O_3 phase in the form of thin parallel and intersecting stripes and needles.

In another study[48] titanium monoxide nanocrystals were produced by high-energy disintegration of pre-synthesized finely dispersed powders of nonstoichiometric titanium monoxide (*B*1-type structure) of different stoichiometry in a Retsch PM 200 planetary ball mill lined with stabilized zirconia. According to X-ray and electron microscopy data, the atomic structure of the titanium monoxide nanoparticles was identical to the parent *B*1-type structure.

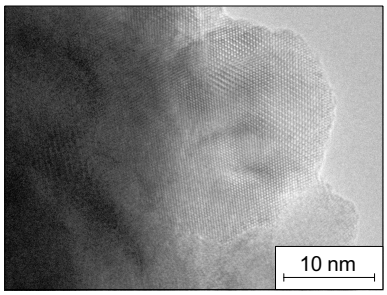


Figure 1. HRTEM image of titanium monoxide nanoparticles prepared by high-energy ball milling. The particle size varies from 20 to 40 nm. From authors' archival materials for Ref. 48.

An analysis of the effect of milling time on the size of the coherent scattering regions (D_{CSR}) treated to a first approximation as the nanoparticle size of nonstoichiometric titanium monoxide showed that the particle size decreased from 25 μm to 20 – 40 nm, while the microstrain (ε) increased from zero to 0.57% after 480-min milling. Experimental data were well fitted by a hyperbolic function which takes account of the initial particle size before milling, the minimum particle size achieved by milling, and the properties of the material (*via* a coefficient related to the softness and brittleness of the material and characterizing the disintegration rate, *i.e*. how rapidly the material can be disintegrated into particles of the minimum size). The particle size determined from the broadening of X-ray diffraction reflections agrees in order of magnitude with the particle size determined by high-resolution transmission electron microscopy (HRTEM) (Fig. 1).

The size of the final nanoparticles depends on the stoichiometry of the initial TiO_y powder. The lattice strain in the nearly stoichiometric ordered monoxide nanoparticles reduces by a factor of 3 compared to the disordered sample. The particle size and lattice strain are plotted *vs*. relative content of oxygen y in Fig. 2. The dependence of D_{CSR} [nm] on y can be described by the linear function

$$D_{CSR}(y) = -45.43 + 69.34\,y \qquad (1)$$

The minimum particle size achieved after 480-min milling is 20 ± 10 nm for the ordered titanium monoxides and

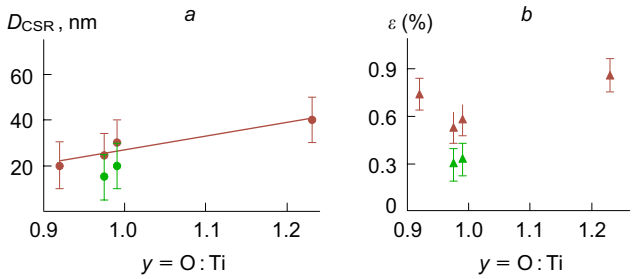


Figure 2. Crystallite size (D_{CSR}) (*a*) and lattice strain (ε) (*b*) plotted *vs*. relative content of oxygen in titanium monoxide TiO_y.[48] Red solid circles and triangles correspond to the disordered samples while green solid circles and triangles correspond to the ordered samples. The minimum nanocrystallite size achieved after 480 min milling is 20 ± 10 nm for ordered titanium monoxides and 40 ± 10 nm for disordered ones. This figure is provided courtesy of Springer Nature.

40 ± 10 nm for the disordered ones; the lattice strain in the former is three times lower than in the latter.

Long-term *in situ* annealings of nanocrystalline TiO_y with cubic (space group $Fm\bar{3}m$) $B1$-type structure prepared by high-energy ball milling led to formation and stabilization of a new ordered orthorhombic (space group *Immm*) nanophase Ti_9O_{10}.[49] Based on analysis of X-ray diffraction data and on estimation of the free energy and stability of the finely dispersed phase Ti_9O_{10} using quantum chemical calculations, the lattice constants and the distribution of atoms and structural vacancies in the titanium and oxygen sublattices were determined (Fig. 3). Quantum chemical calculations of the free energies of micro- and nanophases Ti_9O_{10} showed that only the nanophase is stable owing to a feature of surface relaxation. It is assumed that the Ti_9O_{10} phase is formed only on going from the crystalline state to a nano state.

Stability of mechanically loaded TiO_y nanopowders was studied.[50] High-energy milling of ordered monoclinic (space group $C2/m$) nanocrystals TiO_y led to complete disappearance of long-range order and formation of disordered cubic (space group $Fm\bar{3}m$) phase TiO_y. Subsequent long-term vacuum annealing of nanocrystalline TiO_y at 300 – 1200 K led to formation of ordered orthorhombic (space group *Immm*) phase Ti_9O_{10}. According to electronic structure calculations, the cohesive energy of coarse-crystalline phase Ti_9O_{10} is -14.34 eV, being nearly equal to that of disordered cubic phase $TiO_{1.11}$ (-14.35 eV). It follows that the existence of the coarse-crystalline phase Ti_9O_{10} is energetically unfavourable. It is believed[50] that the formation of orthorhombic phase in nanocrystalline titanium monoxide is due to the size effect on going to the nano state.

A study[51] of the effect of high pressure and temperature on the structure of nanocrystalline monoxide $TiO_{0.98}$ showed that the monoxide structure depends on the experimental conditions. Samples were annealed at a pressure of 6 GPa and at 573, 773, 1273, 1773, 2273 K for 60 min. According to X-ray diffraction data obtained at a pressure of 6 GPa, raising the temperature from 298 to 773 K caused the lattice constant of nanocrystalline TiO_y to change from 417.6 to 417.8 pm (*cf.* the range of 418 – 421 pm for coarse-crystalline titanium monoxide in the same temperature range). The temperature dependence of the lattice constant in nanocrystals at a pressure of 6 GPa is nonmonotonic. Namely, the lattice constant increases in the temperature range of 298 – 773 K, decreases to 417.5 pm at 1273 K and to 416.0 pm at 1773 K and again increases to 417.5 pm at 2273 K, still being somewhat smaller than at 298 K. The temperature range where the lattice constant of the cubic structure monotonically increases corresponds to the one and only initial disordered cubic phase. At $T > 1273$ K, the system becomes two-phase since a trigonal (space group $R\bar{3}c$) phase Ti_2O_3 is formed. Its structure is not derived from the $B1$-structure, being vacancy-free.

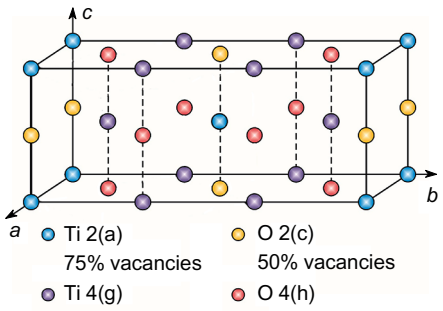


Figure 3. The unit cell of orthorhombic (space group *Immm*) ordered phase of Ti_9O_{10} plotted using the results published in Ref. 49. The types and multiplicities of crystallographic positions of titanium and oxygen atoms are shown.

Ab initio calculations of cohesive energy and electronic structure showed that the formation of this trigonal phase is energetically more favourable than the formation of disordered cubic monoxide of the same composition $TiO_{3/2}$ or orthorhombic (space group *Immm*) ordered phase Ti_2O_3 with a structure derived from the $B1$-type structure. The calculated cohesive energies of the trigonal, disordered cubic and ordered orthorhombic phases are -17.76, -16.21 and -17.25 eV, respectively. The energy distributions of the density of electronic states for the three different structures of the composition $TiO_{3/2}$ suggest[52] that all of them have a metallic-type conductivity; the highest density of states at the Fermi level was found for the orthorhombic phase. Nonmonotonic character of the temperature dependence of the lattice constant is due to the formation of the trigonal phase Ti_2O_3 differing in composition ($TiO_{3/2}$) from the parent disordered cubic phase $TiO_{0.98}$. It was shown[52] that long-term vacuum annealing of nanocrystalline monoxide TiO_y (crystallite size ~ 30 nm) in the temperature range of 300 – 1200 K leads to formation of orthorhombic (space group *Immm*) superstructures Ti_2O_3 and Ti_3O_2.

Recently,[41 – 43] the effect of the properties (composition, crystallite size, degree of ordering) of nanocrystalline monoxide TiO_y on the magnetic susceptibility (χ) of the compound was studied for the first time. *In situ* measurements in the temperature range of 300 – 1200 K revealed that the magnetic susceptibility depends on the stoichiometry, the degree of long-range order and the nanocrystallite size. It was found[41] that the magnetic susceptibility of the ordering titanium monoxide nanocrystals includes three contributions:

(*1*) the contribution from the crystal with the maximum degree of ordering;

(*2*) the Van Vleck contribution depending on the degree of ordering; and

(*3*) the Van Vleck contribution proportional to the number of atoms on the nanocrystal surface.

The study of TiO_y nanocrystals revealed that contribution *2* is proportional to the deviation of the degree of long-range order from its maximum value while contribution *3* is proportional to the specific surface area of nanocrystals. The paramagnetic component of contribution *3* is inversely proportional to the nanocrystal size since reduction of the particle size causes violation of the symmetry of the local environment of the near-surface titanium and oxygen atoms. The contribution *3* to the magnetic susceptibility of TiO_y nanocrystals is related to the specific surface area ($k_{surface}$), density (ρ) and size (D) of the crystal as follows:

$$\chi_{VV}(D) = \frac{6k_{surface}}{\rho D} \qquad (2)$$

More recently,[49, 59] it was proposed that a similar size effect should be observed not only for the monoxide TiO_y in its homogeneity range, but also for paramagnetic nanocrystals of other nonstoichiometric compounds.

Nanocrystalline titanium monoxide was also successfully synthesized using a number of unconventional techni-

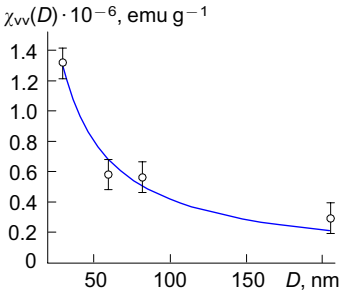


Figure 4. Dimensional Van Vleck contribution $\chi_{VV}(D)$ [see Eqn (2)] to magnetic susceptibility of nanocrystalline monoxide TiO_y ($y \approx 1.1$).[43] The solid line denotes approximation of experimental data by a hyperbolic function. This figure is provided courtesy of Springer Nature.

ques including laser ablation [53, 54] and low-energy ion bombardment.[55] An alternative route to nanocrystalline nonstoichiometric titanium monoxide is to reduce titanium dioxide.[56, 57] In particular, nanocrystalline titanium monoxide was obtained [56] by reducing titanium dioxide (rutile) with magnesium powder. After reduction, the magnesium oxide impurity was removed by acid-base neutralization with dilute hydrochloric acid. At the same time, titanium monoxide present in solution was partially oxidized, so a protective amorphous TiO_{1+x} shell was formed on the surface of TiO nanoparticles. A HRTEM study of the morphology of the $TiO@TiO_{1+x}$ core–shell particles showed that the particle size of titanium monoxide inherited that of the parent rutile nanoparticle (30 – 50 nm) and was not changed upon the reduction. The average thickness of the amorphous shell was 5 nm. It was also reported [56] that nanocrystalline $TiO@TiO_{1+x}$ is a type II superconductor with $T_c = 11$ K. Such an unusual superconductivity can originate from an interface effect due to a linear dependence of the O : Ti ratio in the radial direction.

Hydrothermal treatment of amorphous titanium hydroxide at different temperatures with different isothermal heat-treatment time gave titanium dioxide nanopowders with a crystallite size of 16, 30 and 69 nm.[57, 58] Amorphous titanium hydroxide was preliminarily obtained by redeposition from hexachlorotitanic acid. Titanium dioxide (anatase) nanoparticles were synthesized by hydrothermal treatment of titanium hydroxide in aqueous medium at a pressure of 70 MPa. Different dispersity of nanopowders was specified by the synthesis temperature, namely, 470, 520 and 570 K. The isothermal heat-treatment time was 4 h. Titanium dioxide nanopowders were reduced by heat treatment in a Tamman furnace in hydrogen atmosphere (H_2 flow rate was 5 L min^{-1}). Heat treatment was carried out at 1070, 1170 and 1270 K and the isothermal heat-treatment time was 1, 5.5 and 27.5 h, respectively. This treatment of the TiO_2 (anatase) nanoparticles in hydrogen flow resulted in nanocrystalline nonstoichiometric titanium oxides containing the Magnéli phase Ti_9O_{17} as the major component. The procedure requires the formation of rutile as intermediate phase.[57] The degree of crystallinity of the Ti_9O_{17} nanopowders depends on the crystallite size of rutile.

Thermodynamic calculations of TiO_2 reduction with hydrogen in the temperature range of 500 – 3000 K at equilibrium concentrations of reduction products and at $TiO_2 : H_2$ molar ratios of $1 : 10^n$ ($n = 1 – 6$) were carried out [57] using the IvtanThermo software package. According to calculations performed with allowance for experimental data, reduction of TiO_2 begins at temperatures from 600 to 1200 K depending on the concentration of hydrogen in the reaction medium (Fig. 5) and results in the oxides Ti_4O_7, Ti_3O_5, Ti_2O_3 and TiO. Under the experimental conditions,

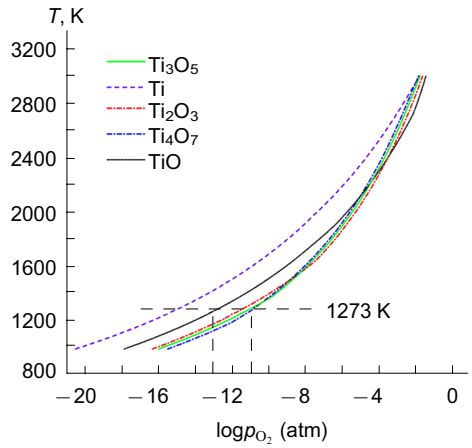


Figure 5. Regions of equilibrium coexistence of titanium oxides in the $\log p_{O_2} - T$ coordinates. Calculated by the authors of this review using the data taken from Ref. 57.

the lower temperature boundary of TiO_2 reduction was ~1270 K. This temperature can be decreased by increasing the H_2 flow rate. The degree of TiO_2 reduction depends on the partial pressure of oxygen; therefore, the regions of equilibrium coexistence of major reduction products were also calculated additionally. Our calculations using the data taken from Ref. 57 showed that a complete reduction of TiO_2 to TiO with isothermal heat-treatment at ~1273 K requires that the partial pressure of oxygen be at most 10^{-13} atm (see Fig. 5).

The reduction conditions were chosen based on the results of thermodynamic calculations, and TiO_2 nanopowders with different crystallite size (19, 27 and 36 nm) were then reduced in a Tamman furnace in H_2 atmosphere at 1070, 1170, 1270 and 1370 K with isothermal heat-treatment times from 1 to 27.5 h. It was found that the order of physicochemical transformations occurring in the course of TiO_2 reduction with hydrogen depends on the nature of the initial composition. Reduction of titanium oxyhydroxide at 1070 K was accompanied by observation of TiO_2 (rutile) reflections in the X-ray diffraction pattern. Raising the temperature to 1170 K was accompanied by an increase in the average crystallite size of rutile. At 1270 K, the rutile diffraction reflections disappeared and reflections corresponding to the Magnéli phases Ti_nO_{2n-1} ($4 \leqslant n \leqslant 9$) with Ti_9O_{17} as the major component appeared.[57] The formation of anatase crystallites at most 50 nm in size during the reduction of TiO_2 nanoparticles of different size at 1070 K was observed. As the temperature increased to 1170 K, anatase transformed to rutile with preservation of the average crystallite size. On further heating to 1270 K rutile underwent a complete transformation to the Magnéli phases with major content of the Ti_9O_{17} phase. The average crystallite size of the Ti_9O_{17} phase formed in the reduction of TiO_2 nanoparticles was much larger than in the reduction of titanium hydroxide. Raising the reduction temperature to 1370 K and an increase in the isothermal annealing time led to formation of more oxygen-deficient Magnéli phases up to the oxide Ti_3O_5. Based on the results of experimental studies and calculations, a scheme was proposed of physicochemical transformations occurring during the reduction of titanium hydroxide or anatase (Fig. 6).

Additional thermodynamic calculations of the formation of nonstoichiometric titanium oxides using other

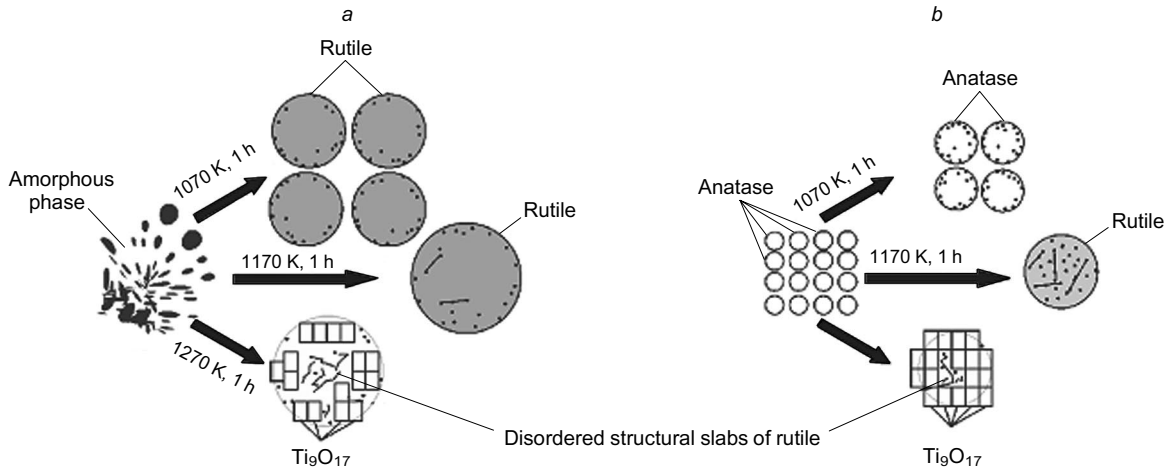


Figure 6. Schemes of physicochemical transformations of titanium hydroxide (*a*) and anatase (*b*) nanoparticles upon heat treatment in hydrogen flow.[57] This figure is provided courtesy of Springer Nature.

reducing agents revealed the possibility of further reduction of TiO_2 to Magnéli phases of the composition $TiO_{1.75-1.89}$ under milder thermal conditions that exclude the growth of titanium dioxide nanocrystals. Not only H_2, but also such gases as CO, CH_4 and NH_3 were considered as reducing agents. It was found that the reducing capacity increases as follows: $CO < H_2 < CH_4 < NH_3$. For instance, the temperature of the onset of reduction of titanium dioxide with NH_3 at 1 atm hydrogen pressure can decrease by 400 K; it can also be decreased using more dispersed TiO_2.

A positron lifetime spectroscopy study [59] showed that free surface of TiO_y nanocrystals and nanocrystal/nanocrystal interfaces have defect structures. This method allows one to detect vacancies inside nanoparticles, at interfaces and on the free surface of nanoparticles. An analysis of the positron lifetime spectra of TiO_y nanocrystals revealed a short-lifetime and a long-lifetime component. The former (lifetime 205 ps, intensity 62%) corresponds to the localized trap state of a single titanium vacancy. The latter (lifetime 349 ps, intensity 38%) corresponds to the localized state of positron trapping at grain boundaries. The average size of TiO_y nanocrystals studied varied from 20 to 40 nm, being in the range of average diffusion lengths of thermalized positrons; therefore, the probability of positron annihilation on the surface and at interfaces between nanoparticles is very high. Based on the results of determination of the positron lifetimes, it was assumed [59] that the shorter the distance from the surface of nanocrystals the lower the concentration of titanium vacancies in TiO_y. Thus, a gradient of the concentration of structural vacancies appears on going from the surface to the bulk of TiO_y nanocrystals, and the smaller the nanocrystals the higher the concentration gradient.

The effect of the nanoparticle size on the amount of structural vacancies in the monoxide TiO was studied [60] quantum chemically in terms of the density functional theory using the tight-binding approximation. According to calculations, the thermodynamic stability of TiO nanoparticles depends only slightly on their shape but noticeably increases with increasing the nanoparticle size. The role of the surface of titanium monoxide nanoparticles in stabilizing the TiO composition, is just like that of structural vacancies in the coarse-crystalline monoxide. Therefore, the concentration of vacancies in large TiO nanoparticles should be lower than in coarse-crystalline titanium monoxide. In other words, the larger the size and surface area of a titanium monoxide nanoparticle the lower the concentration of structural vacancies in the nanoparticle. The thermal stability of the morphology of TiO nanoparticles was studied by the molecular dynamics method. A simulation showed that $Ti_{97}\blacksquare_{11}O_{97}\square_{11}$ nanoparticles containing structural vacancies are characterized by higher structural rigidity and smaller distortions on heating to higher temperatures compared to the defect-free cubic ($Ti_{108}O_{108}$) and spherical ($Ti_{140}O_{140}$) nanoparticles.

2.2. Titanium dioxide

There are three crystalline polymorphs of titanium dioxide TiO_2:

— tetragonal (space group $P4/mnm$) — rutile,
— tetragonal (space group $I4_1/amd$) — anatase, and
— orthorhombic (space group $Pcab$) — brookite.

The most abundant polymorph, rutile, has a stoichiometric composition at 300 K. It was reported [61, 62] that at $T > \sim 1000$ K, rutile has a defect structure with vacancies in the oxygen sublattice and is characterized by a narrow homogeneity range from TiO_{2-x} ($2-x = 1.983-1.992$) to TiO_2. In addition, single-phase rutile exists in the composition range from $TiO_{1.96}$ to TiO_2 at 1370 K and from $TiO_{1.93}$ to TiO_2 at 1500 K.[63]

Titanium dioxide with oxygen vacancies can be obtained by growing nanofilms on titanium foil.[64, 65] In this case nonstoichiometric titanium dioxide is formed at the contact between stoichiometric titanium dioxide and metallic titanium.

Titanium dioxide nanotube films were fabricated [66 – 69] by electrochemical anodization using a titanium foil 100 μm thick. Pre-anodization in a 1% solution of hydrofluoric acid in ethylene glycol for 20 min at room temperature was followed by etching the titanium foil in a mixture of nitric and hydrofluoric acids for 3 min. Secondary anodizations were performed in a 1% solution of NH_4F in ethylene glycol at a voltage of 20 V for 15, 30, 60, 120, 180 and 360 min. The process resulted in a titanium dioxide nanotube film. The nanotubes were from 500 nm to 2 μm long and had inner diameters in the range of 30 – 40 nm and outer diameters ranging from 45 to 55 nm (Fig. 7). The largest surface area of the nanotubes was achieved after 120 min of anodization.

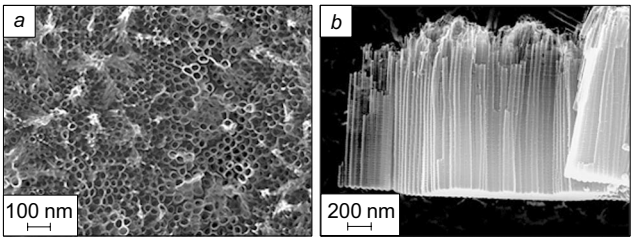


Figure 7. Scanning electron microscopy (SEM) images of nanotube TiO_2 film prepared by anodization for 120 min.[66] Top view (*a*) and side view (*b*). This figure is provided courtesy of Springer Nature.

A small-angle ($18^\circ < 2\theta < 33^\circ$) X-ray study of the titanium dioxide nanotube film revealed an intense diffuse halo with a maximum at $\sim 25^\circ$. This fact on the one hand and the absence of diffraction reflections in the same 2θ range on the other hand suggest that the nanotube film is amorphous.

The titanium dioxide nanotube film was studied by optical diffuse reflectance spectroscopy, and a broad blurred reduction of diffuse reflection was observed at $\lambda \geqslant 450$ nm. Earlier, an experimental study of films by energy-dispersive X-ray spectroscopy (EDX) and photoelectron spectroscopy,[67,68] together with thermodynamic calculations unambiguously demonstrated that the film composition deviates from stoichiometric. Vacancies create additional energy levels in the band gap of TiO_2, which leads to noticeable absorption of visible light at $\lambda \geqslant 450$ nm.

The maximum band gap (E_g) of the titanium dioxide nanotube film fabricated by anodization for 120 min is ~ 3.3 eV *vs.* 3.0 eV for the TiO_2 nanopowder (Degussa P25). The nanotube film also contains nonstoichiometric oxide phases with a narrower band gap (~ 2.8 eV).

The reduction of optical diffuse reflection and the absorption of visible light at $\lambda = 450$ nm are evident proofs of catalytic activity of the TiO_2 nanotube film. The catalytic activity of the film was determined using the oxidation of acetone vapours to CO_2 over the film and, for the sake of comparison, over titanium dioxide powder (Degussa P25) supported on a glass substrate. Photocatalytic measurements were carried out under irradiation with visible light at $\lambda = 450$ nm. Experiments[66] demonstrated that the catalytic activity of the nanotube film is twice as high as that of the TiO_2 powder (Degussa P25). Enhanced catalytic activity of the titanium dioxide nanotubes under irradiation with visible light is due to (i) nonstoichiometry of TiO_2 near the interface between the nanotubes and the titanium foil (substrate) and (ii) well-developed surface. More efficient absorption of visible light owing to the presence of vacancies in the oxygen sublattice leads to significant enhancement of photocatalytic activity.

It was reported[67] that raising the calcination temperature causes the optical band gap of the nanotube films to narrow since the stoichiometry and phase composition change. In particular, the photocatalytic activity of the film calcined at 773 K is four times higher than that of commercially available TiO_2.

Integrated studies[64–69] showed that nanostructured nonstoichiometric titanium dioxide is non-toxic, environmentally safe and economically affordable material which can be used as 'green' photocatalyst for the synthesis of organic compounds for medicine.

Xerogels based on titanium dioxide and its compositions are of considerable interest to both basic research and applied studies. They are widely used in different industries. Particular application fields of TiO_2 xerogels are determined by the particle shape and size, the phase composition, the pore diameter and structure and the specific surface area. These parameters depend strongly on the xerogel preparation method. For instance, TiO_2 and TiO_2-SiO_2 xerogels with 3D globular porous structure and narrow globule size distribution were synthesized[70] by hydrolysis of tetrabutoxytitanium and its mixture with tetraethoxysilane in the acetic acid (vapour) – H_2O atmosphere followed by calcination. The synthesis in the presence of acetic acid vapours facilitated the formation of a TiO_2 xerogel with extended specific surface area.

We have considered only two representatives of a vast variety of nonstoichiometric oxides. Titanium dioxide and titanium monoxide belong to the Ti–O system, one of the most practically important oxide systems, and are relevant examples of nonstoichiometric oxides. By varying the concentration of structural vacancies, heat treatment regimes and by controlling the particle size, one can obtain titanium dioxide and titanium monoxide with specified chemical and physical properties. These compounds are of interest from the standpoint of both fundamental research and practical applications. Nanocrystalline titanium monoxide is a promising material for manufacturing single-electron transistors[71] in order to achieve further miniaturization of nanoelectronics devices.

Researchers pay considerable attention to nanostructured nonstoichiometric titanium dioxide TiO_2 with well-developed surface and specific morphology as efficient functional material with a wide range of applications, especially, as photocatalyst. The advantage of nonstoichiometric titanium dioxide as photocatalyst over stoichiometric TiO_2 consists in that it is catalytically active under irradiation with visible light, which excludes the use of UV irradiation. Going from stoichiometric to nonstoichiometric titanium dioxide is due to the appearance of structural vacancies in the oxygen sublattice. Consequently, the atomic structure changes, additional energy levels appear within the band gap and the effective band gap narrows. These factors affect the electronic, optical and catalytic properties of the material. Nonstoichiometric titanium dioxide as photocatalyst can be used for wastewater treatment to remove organic impurities, in hydrogen power engineering and for 'green' synthesis of drugs in medicinal chemistry.

2.3. Effect of nonstoichiometry and size of TiO_y nanoparticles on the structure and properties of hydroxyapatite-based nanocomposites

The results of successful studies of nanomaterials form a basis for the design of novel functional nanocomposite materials based on the available compounds. A large number of phosphates including those used in medicine belong to the $CaO-P_2O_5$ system. Synthetic hydroxyapatite (HAp) $Ca_{10}(PO_4)_6(OH)_2$ is one of the most widely used phosphates utilized for bone defect replacement and for coating implants to improve adhesion to bone tissue. However, low mechanical strength and cracking resistance make bioceramics of limited use. Mechanical properties are improved using zirconium, titanium and titanium dioxide additives.[72–76] Titanium and its oxides are characterized by

good biocompatibility, their addition to bioceramics improves the mechanical strength and cracking resistance [73] and causes the onset of photocatalytic activity [74] and bactericidal properties. It was found [76] that the HAp/TiO_2 composite is suitable for efficient degradation of pentachlorophenol while the HAp/Ti nanocomposite [77] can be used to remove dyes from aqueous solutions. In addition, nanostructured composite materials based on HAp demonstrate enhanced biological activity compared to analogous compositions containing microparticles.[73]

When fabricating and studying bioceramics, researchers pay careful attention to stoichiometry of the matrix material, in particular, hydroxyapatite. A significant role is played by the Ca : P ratio, which to a great extent predetermines the dissolution rate of the phosphate. For hydroxyapatite, the stoichiometric ratio is 1.67. It is this calcium-to-phosphorus ratio that corresponds to the highest thermal stability of HAp, its stability to various types of heat treatment and solvent stability; ceramics based on stoichiometric HAp exhibits better mechanical properties and is characterized by the highest density, hardness and flexural strength.[78] However, until recently there has been lack of attention to the influence of stoichiometry of modifying agents.

Recent studies showed that nonstoichiometry significantly influences the properties of the final nanocomposite even if the nonstoichiometric material is present as an additive (10 – 20 mass%). For instance, the effect of substoichiometric monoxide $TiO_{0.92}$ (10 and 20 mass %) on the properties of a nanocomposite material based on HAp was studied.[79] Nanoceramics was prepared by mixing nanopowdered initial materials in a planetary ball mill, pressed and annealed *in vacuo* (10^{-3} Pa) at 670 and 870 K. A thorough examination of the morphology, microhardness, specific surface area, density, shrinkage, mass loss and phase composition of the samples in each step of the synthesis procedure revealed the order of physicochemical transformations and the role of the nonstoichiometry of the additives. In the presence of additives, the porosity was reduced in the nanopowder mixing step, so no volume expansion was observed during the annealing. Based on powder X-ray diffraction data, annealing at 670 K is followed by the oxidation of titanium monoxide to titanium dioxide, which is formed at 870 K. Under oxygen-deficient conditions (vacuum annealing) in the presence of 10 mass % $TiO_{0.92}$, the oxidation occurs through the uptake of oxygen from HAp. As the content of the additive increases to 20 mass%, the amount of available oxygen becomes insufficient for complete oxidation of $TiO_{0.92}$ to TiO_2; as a consequence, two intermediate phases, $Ti_{4.5}O_5$ and Ti_6O_{11}, are formed in addition to TiO_2 (anatase).

The unit cell of hydroxyapatite $Ca_{10}(PO_4)_6(OH)_2$ contains 75 Ca – O bonds, 24 P – O bonds, 6 Ca – OH^- bonds and two O – H^- bonds.[80] Probably, the oxidation of titanium monoxide occurs through uptake of oxygen ions from hydroxyl groups of HAp. X-Ray diffraction data showed that the crystal structure of HAp remains unchanged, although oxygen vacancies appear. This can lead to changes in the phase composition of components on heating to higher temperatures and to decomposition of HAp. The nanostructure of the annealed composite material persists.

The addition of $TiO_{0.92}$ leads to a decrease in the hardening onset temperature of the composite material by 200 – 250 K compared to that of pure HAp. An increase in the amount of $TiO_{0.92}$ causes the formation of new phases, namely, $Ti_{4.5}O_5$ (Ti_9O_{10}) and Ti_6O_{11}, during the annealing. This in turn leads to changes in the properties of the final composite material. These three phases are ordered, thus being relatively more thermodynamically stable than the disordered phases of the Ti – O system, which can be formed in the course of annealing. A feature of the ordered phase Ti_6O_{11} is that it has planes of easy slip. This can facilitate the slip of defects towards grain boundaries, accumulation of dislocations in the bulk and at grain boundaries, as well as strengthening of the material.

The addition of the same amounts of superstoichiometric $TiO_{1.23}$ causes temperature-dependent changes in the microhardness, density and specific surface area of nanocomposites.[81] A complete oxidation results in TiO_2 (rutile). The maximum microhardness of the nanocomposite material was achieved in the presence of 20 mass% $TiO_{1.23}$, while the composite containing 20 mass% $TiO_{0.92}$ had the maximum density. Nonstoichiometry of the titanium monoxide additives affects the intensity of secondary crystallization of HAp on annealing (Fig. 8). It should be noted that nonstoichiometry of TiO_y influences the TiO_2 polymorph. In the case of substoichiometric composition TiO_y, oxygen deficiency and the formation of intermediate phases preclude the anatase – rutile transition.

A Raman spectroscopy study [83] of the structure of HAp/TiO_y nanocomposites showed that annealing of samples at 670 K is followed by changes in the valence state of titanium, formation of surface groups $[Ti(OH)_2]^{2+}$ and $[TiHPO_4]^{2+}$ corresponding to peaks in the region of 3751 – 3902 cm^{-1} in the IR spectra and partial cationic heterovalent substitution Ti^{3+} and Ti^{4+} cations for Ca^{2+}. As the annealing temperature increases to 870 K, peaks in the region of 3751 – 3902 cm^{-1} are no longer observed, thus indicating disappearance of the surface groups. In the case of the HAp/$TiO_{0.92}$ nanocomposite, no complete oxidation of the monoxide $TiO_{0.92}$ to TiO_2 occurred under the oxygen-deficient conditions; however, an intermediate nanophase $Ti_{4.5}O_5$ was formed. Annealing of the HAp/$TiO_{1.23}$ nanocomposite at 870 K gave TiO_2.

The microstructure of HAp/TiO_y nanocomposites containing $TiO_{0.92}$ and $TiO_{1.23}$ (10 and 20 mass % in both cases) was studied in detall.[84, 85] A mixture of HAp and TiO_y nanopowders was exposed to high-energy milling followed by annealing. According to SEM data, the resulting nanocomposite contained cylindrical HAp nanoparticles ~10 nm in diameter and up to 100 nm long; heating with an electron beam led to partial decomposition of HAp on the surface of nanoparticles with the formation of CaO. Annealing of the HAp/TiO_y nanocomposites at 673 and 873 K led to formation of different phases depending on the

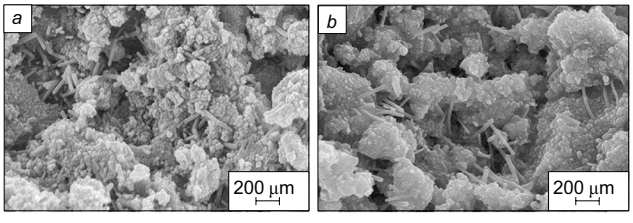


Figure 8. SEM images illustrating the result of secondary crystallization of HAp/TiO_y nanocomposite upon annealing at 670 K: HAp/10 mass % $TiO_{0.92}$ (*a*) and HAp/10 mass % $TiO_{1.23}$ (*b*). From authors' archival materials for Refs 81 and 82.

composition of the titanium monoxide additive and on the composition of the final nanocomposite. In particular, annealing of the nanocomposite at 873 K afforded TiO_2 (rutile) as a result of the oxidation of TiO_y.

It was concluded [85] that nonstoichiometry of TiO_y additives affects the formation of new phases $Ti_{4.5}O_5$ and TiO_2 in HAp/TiO_y nanocomposites and the phase composition of the nanocomposites in different steps of annealing.

By and large, it was shown [81–85] that nonstoichiometry of the titanium monoxide additive significantly influences the properties of the end product, HAp/TiO_y nanocomposite, and the role of nonstoichiometry cannot be ignored. We believe that progress in this field will offer prospects for not only the design of materials with predictable properties, but also for targeted variation of the properties. In particular, by varying the nonstoichiometry of the modifying agent (additive) one can change the morphology and properties of the HAp/TiO_y nanocomposite in targeted manner.

3. Nanocrystalline nonstoichiometric carbides

Cubic Group IV and V transition-metal carbides are highly nonstoichiometric compounds [86] with the widest homogeneity ranges among all known compounds. Their hardness approaches that of diamond.

High-energy milling is one of the main routes to nanocrystalline carbide powders.[87–89] Carbide nanopowders and nanotubes are also prepared by low-temperature synthesis, thermal decomposition and other techniques.[90–93] The most informative methods for studying the atomic structure and microstructure of carbide nanoparticles include X-ray diffraction and neutron diffraction.

Disordered cubic (space group $Fm\bar{3}m$) vanadium carbide VC_y with a $B1$-type structure is of particular interest. Its homogeneity range spans from $VC_{0.65}$ to $VC_{0.875}$, the upper boundary being far from the stoichiometric composition $MC_{1.0}$.[94–97] Ordered phases V_8C_7, V_6C_5 and V_3C_2 can be formed in the homogeneity range of vanadium carbide.[94, 95, 98, 99]

Studies [95, 100] of coarse-crystalline ordered carbide $VC_{0.875}$ revealed no homogeneity range for the ordered cubic (space group $P4_332$) phase V_8C_7. In addition, no indications of displacements of carbon atoms from sites of a perfect lattice of V_8C_7 were observed.[100] However, the authors of X-ray diffraction studies [94, 95] of coarse-crystalline phase V_8C_7 reported large atomic displacements of both metal and nonmetal atoms. It was found that vanadium and carbon atoms are displaced towards the vacant site □ of the nonmetal sublattice, the displacements of carbon atoms being larger than those of vanadium atoms. The X-ray diffraction [95, 98] and neutron diffraction [99, 100] estimates of atomic displacements differ appreciably. In this connection the effect of the particle size of nanocrystalline dispersed ordered carbide V_8C_7 on the possible appearance of a homogeneity range of the ordered phase and on atomic displacements in the nanoscale superstructure V_8C_7 was experimentally studied [101] by X-ray diffraction, time-of-flight (TOF) neutron diffraction, SEM and TEM. Nanopowders of ordered vanadium carbide were prepared by high-energy milling of coarse-crystalline ordered carbide V_8C_7.[101]

The neutron diffraction patterns of this powder demonstrated reflections from disordered carbide and weak superstructural reflections from the ordered phase V_8C_7 (Fig. 9). The intensities of the superstructural reflections depended

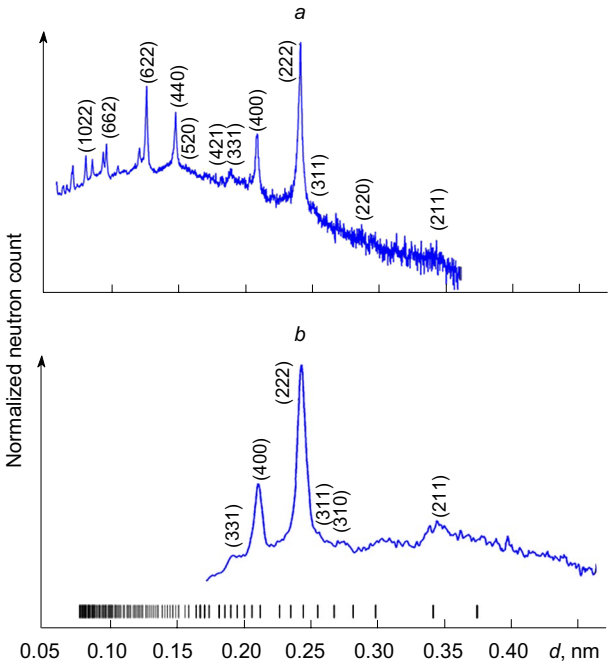


Figure 9. Neutron diffraction patterns of $\sim V_8C_7$ nanopowder recorded using HRFD detectors arranged at the scattering angles of 152° (*a*) and 90° (*b*).[101] The nanopowder was prepared by 10 h high-energy milling of coarse-crystalline powder. Vertical bars denote the positions of diffraction reflections of the V_8C_7 superstructure. This figure is provided courtesy of Elsevier.

on the spectrum recording mode. High-resolution diffraction patterns exhibit weak superstructural reflections in the region $d_{hkl} > 0.25$ nm (Fig. 9 *a*), whereas low-resolution ones clearly demonstrate superstructural reflections (211), (310) and (311) in the same region (Fig. 9 *b*).

A quantitative analysis of the neutron diffraction patterns showed that both coarse- and nanocrystalline vanadium carbide powders contain the ordered phase V_8C_7 and the disordered phase $VC_{0.875}$. Milling was followed by an increase in the content of the disordered phase from 21 ± 3 to 41 ± 10 mass% since the milling energy is very high (170 kJ mol^{-1} for 10-h milling), which exceeds the energy of the order – disorder transition $V_8C_7 \rightarrow VC_{0.875}$.

The results of a TEM study of nanocrystalline vanadium carbide powder confirmed inhomogeneous microstructure of the nanopowder, which is due to the presence of ordered and disordered phases. Figure 10 clearly demonstrates that nanopowder prepared by 15-h milling contains inclusions of the disordered carbide $VC_{0.875}$ ($\sim 8-10$ nm in size) in the matrix of the ordered phase V_8C_7. After annealing at 1070 K, this nanopowder contains only the ordered phase V_8C_7. According to EDX data, the contents of vanadium and carbon in the ordered phase are ~ 79.1 and ~ 16.5 mass%, respectively, which corresponds to carbide of approximate composition $VC_{0.87-0.88}$.

The lattice constants of cubic unit cells of the ordered (V_8C_7) and disordered ($VC_{0.875}$) phases in the vanadium carbide nanocrystalline powder are respectively 0.83268(3) and 0.41466(4) nm, being slightly smaller than those in the coarse-crystalline powder. The occupancy of the 4(*a*) positions in the nanocrystalline superstructure by carbon atoms is ~ 0.97.[99, 101] Thus, the ordered nanophase has the composition $\sim V_8C_{6.97}$ ($\sim VC_{0.871}$) or $V_8C_{7-\delta}$, where $\delta \approx 0.03$.

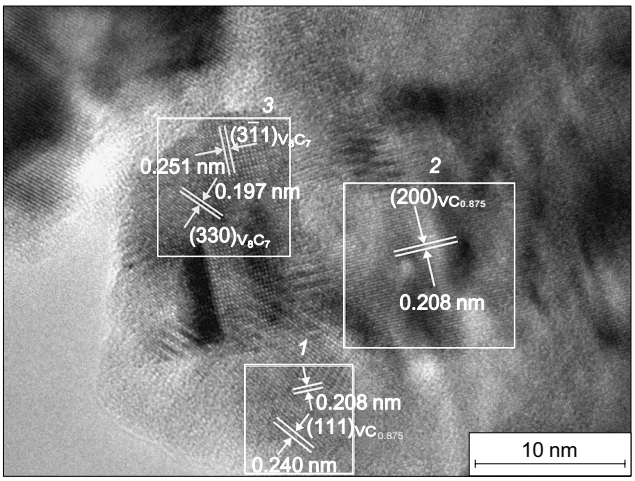


Figure 10. TEM image of nanocrystalline vanadium carbide prepared by 15-h ball milling.[101] The sample contains inclusions (*1*) and (*2*) of disordered carbide $VC_{0.875}$ of size about 8 – 10 nm in the matrix of the ordered phase V_8C_7 (shown is region (*3*) of the ordered carbide V_8C_7, the zone axis of the matrix [$1\bar{1}\,4$]). This figure is provided courtesy of Elsevier.

The atomic displacements of C3 and C4 in the lattice of the nanocrystalline superstructure $V_8C_{7-\delta}$ are small, although being larger than those in the coarse-crystalline superstructure (Table 1) due to noticeable deformation distortions of the lattice that appeared during high-energy milling.

The real structure of the cubic ordered phase $V_8C_{7-\delta}$ in nanocrystalline vanadium carbide (see Table 1) is characterized by small atomic displacements of V1, V2, C3 and C4 from the lattice sites of perfect ordered phase V_8C_7. The local environment of vacant sites in the carbon sublattice is formed by the V2 atoms displaced towards the vacancy. In a perfect superstructure V_8C_7, all V – V distances are equal to 0.2946 nm, whereas in the real superstructure $V_8C_{7-\delta}$ they vary from 0.2883 to 0.3058 nm. Consider the magnitude and direction of atomic displacements in the real superstructure $V_8C_{7-\delta}$ in the $(001)_{B1}$ plane or in the equivalent $(00z)$ plane with $z \approx 0.625$ of the V_8C_7 phase. The distribution of atomic displacements in the $(00z)$ plane with $z \approx 0.625$ according to neutron diffraction data,[99, 101] X-ray diffraction data[98] and calculations[102] is shown in Fig. 11. For clarity, the atomic displacements are multiplied by a factor of 100. A complicated character of symmetry and displacements (see Fig. 11 *a*,*b*) is due to the presence of screw rotations 4_3 corresponding to the rotational symmetry element h_{15} in the cubic ordered phase $V_8C_{7-\delta}$.[6, 16] According to TOF neutron diffraction data, the atomic displacements in the $(00z)$ plane are nearly zero for C3, ~0.0033(2) nm for C4, ~0.0053 for V1 and ~0.0055 nm for V2 (see Fig. 11 *a*).

The atomic displacements in the $(00z)$ plane of the superstructure V_8C_7 determined from X-ray diffraction data are shown in Fig. 11 *b*. It was reported[95, 98] that the atomic displacement of C4 calculated from X-ray diffraction data is ~0.058 nm, which is nearly 18 times larger than the displacements of the same carbon atoms obtained from neutron diffraction data. This seems to be improbable. Indeed, the atomic displacements of C3 are small.[98] One can assume that the difference between the results of X-ray diffraction studies[95, 98] and neutron diffraction measure-

Table 1. Atomic coordinates in cubic (space group $P4_332$) superstructure $V_8C_{7-\delta}$ ($\delta \approx 0.03$) of nonstoichiometric vanadium carbide.[101]

Atom	Positon and multiplicity	Atomic coordinates in coarse-crystalline ordered phase [a = 8.3291(1) Å]			Atomic coordinates in nanocrystalline ordered phase [a = 8.3268(3) Å]			Occupancy
		x/a	x/a	y/a	x/a	y/a	z/a	
C1 (vacancy)	4(*b*)	0.6250	0.6250	0.6250	0.6250	0.6250	0.6250	0
C2	4(*a*)	0.1250	0.1250	0.1250	0.1250	0.1250	0.1250	~0.97
C3	12(*d*)	0.1250	0.6248(2)	0.6252(2)	0.1250	0.6266(12)	0.6234(12)	1.0
C4	12(*d*)	0.1250	0.3720(2)	0.8780(2)	0.1250	0.3686(12)	0.8814(12)	1.0
V1	8(*c*)	0.3705	0.3705	0.3705	0.3705	0.3705	0.3705	1.0
V2	24(*e*)	0.126	0.3815	0.128	0.126	0.3815	0.128	1.0

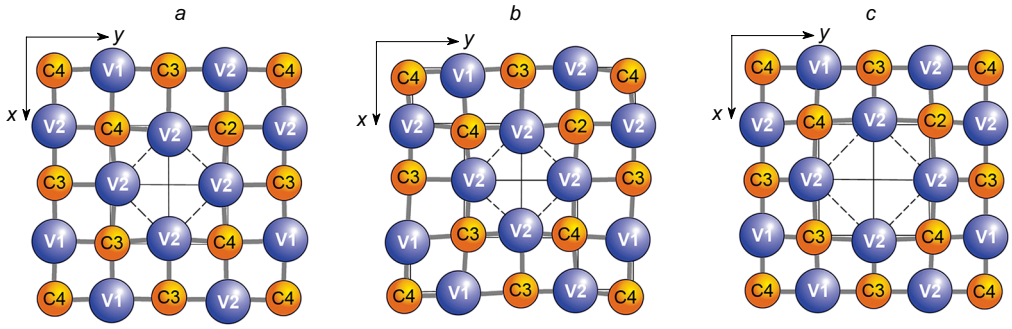


Figure 11. Atomic displacements of vanadium and carbon near the vacant sites in the $(00z)$ plane with $z \approx 0.625$ of the V_8C_7 phase: neutron diffraction data (*a*),[99, 101] X-ray diffraction data[98] for the coarse-crystalline ordered phase V_8C_7 (*b*), and results of calculations (*c*).[102] For clarity, the atomic displacements are multiplied by a factor of 100. The ideal atomic network of the *B*1-type structure is shown by the thin solid line, atoms are enumerated according to Table 1, the cross-sections of the vacant octahedra $\square V_6$ by the $(00z)$ plane are shown by dashed lines. This figure is provided courtesy of Springer Nature.

ments [99, 101] is due to different particle size of the V_8C_7 phase since the X-ray diffraction measurements [95, 98] were carried out using coarse-crystalline sintered samples of the ordered phase V_8C_7, while neutron diffraction measurements [95, 98] were performed using nanocrystalline powders.

Experimental data [99, 101] are in complete contradiction to the results of theoretical calculations [102] of atomic positions in the V_8C_7 superstructure. The principal conclusion drawn in Ref. 102 is that vanadium atoms are displaced away from the vacancy (see Fig. 11 *c*). Contrary to this, it was shown [99, 101] that the V2 atoms representing the environment of the $\square V_6$ vacant sites approach the vacancy. In the real superstructure $V_8C_{7-\delta}$, this increases the electron density at the 4(*b*) vacancy, whereas calculations [102] predict a zero electron density for structural vacancies in the carbon sublattice of perfect V_8C_7 phase. Nonzero electron density at vacancy positions of the cubic superstructure V_8C_7 and positron trapping by vacancies were experimentally confirmed by positron lifetime measurements.[103]

A detailed study of the atomic structure of nanocrystalline cubic ordered phase of vanadium carbide (see above) showed that its composition, $V_8C_{7-\delta}$ (where $\delta \approx 0.03$), differs from the stoichiometric composition V_8C_7 of perfect superstructure. In the ordered nanocrystalline phase $V_8C_{7-\delta}$ six vanadium atoms surrounding any vacant site in the carbon sublattice form clusters $\square V_6$ where vanadium atoms are displaced towards vacant sites.

A correlation between the size and composition of carbide nanoparticles was established by TOF neutron diffraction using nonstoichiometric carbide NbC_y ($y = 0.77$, 0.84, 0.93, 0.96) nanopowders. The processing of TOF neutron diffraction data was described in detail [104] taking carbide $NbC_{0.93}$ as an example. Generalized results of neutron diffraction studies of carbides NbC_y of different composition are available elsewhere.[105] Nanocrystalline powders were prepared by high-energy milling of coarse-crystalline powders of carbides NbC_y ($y = 0.77$, 0.84, 0.93, 0.96) with an average particle size of 2 – 3 μm; milling duration was 5, 10 and 15 h.

High-resolution neutron diffraction patterns of coarse- and nanocrystalline powders of nonstoichiometric carbides NbC_y were collected on a TOF high-resolution Fourier diffractometer (HRFD) [106] at the IBR-2 pulsed reactor (Joint Institute for Nuclear Research, Dubna, Russia) at room temperature. Changes in the neutron diffraction patterns of the initial coarse- and nanocrystalline powders NbC_y milled for 5, 10 and 15 h are illustrated in Fig. 12. Although ordered phases can form in nonstoichiometric carbide $NbC_{0.83}$ and in the composition range $NbC_{0.81-0.88}$ under particular conditions,[86, 107] the neutron diffraction patterns of the initial powders NbC_y showed only diffraction reflections from cubic niobium carbide and no superstructural reflections. Large broadening of diffraction reflections of the nanopowders and an increase in the diffuse background are due to milling and deformation distortions.

A quantitative analysis of the results of neutron diffraction measurements using NbC_y nanocrystalline powders

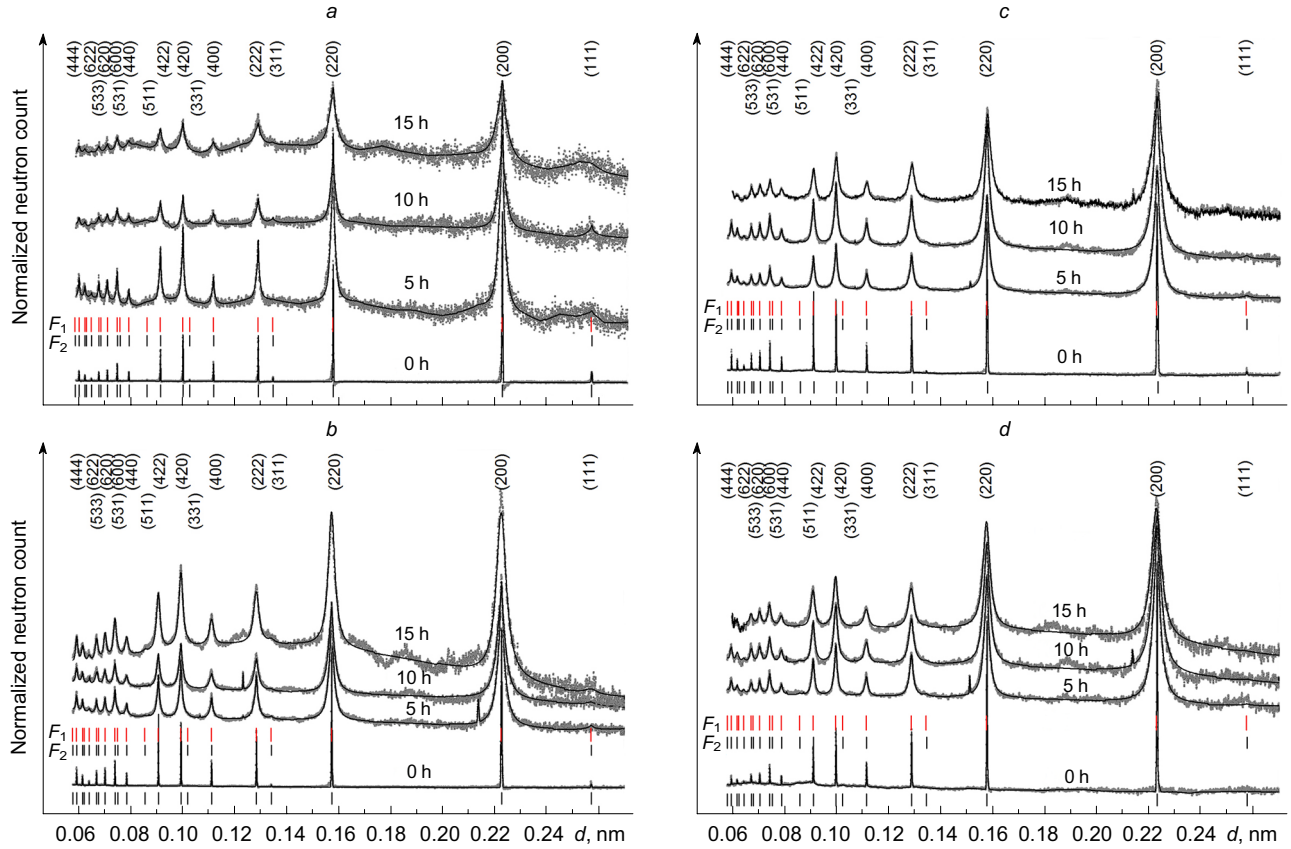


Figure 12. HRFD neutron diffraction patterns of coarse-crystalline and nanocrystalline NbC_y powders prepared by milling over a period of 5, 10 and 15 h: $y = 0.77$ (*a*), 0.84 (*b*), 0.93 (*c*), and 0.96 (*d*).[105] Shown are experimental (points) and calculated (solid lines) neutron diffraction patterns. The upper and lower rows of vertical bars correspond to the calculated positions of the diffraction reflections of nanocrystalline (F_1) and coarse-crystalline (F_2) fractions, respectively. This figure is provided courtesy of Elsevier.

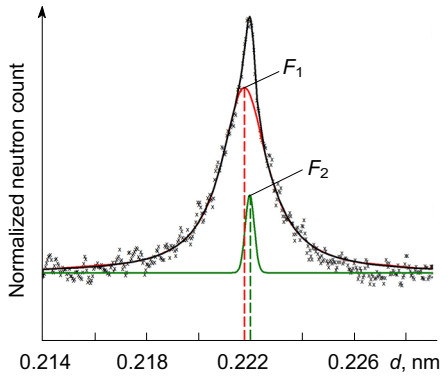


Figure 13. The (200) diffraction reflection of $NbC_{0.77}$ nanopowder prepared by milling over 5 h and its expansion into peaks corresponding to cubic fractions F_1 and F_2 of niobium carbide with different lattice constants (0.44334 and 0.44388 nm), composition ($\sim NbC_{0.76}$ and $\sim NbC_{0.79}$) and average particle size (35 and 150 – 180 nm), respectively.[105] This figure is provided courtesy of Elsevier.

showed that the diffraction reflection profiles can be best fitted assuming that nanopowders contain two cubic fractions of different compositions, lattice constants, and average particle size. As an example, Fig. 13 presents the (200) reflection profile of the $NbC_{0.77}$ nanocrystalline powder. The (200) reflection is a superposition of two peaks, a narrow and a broad one. The major contribution (> 92%) to the reflection comes from the broad peak corresponding to the nanoscale fraction F_1 with a lattice constant of 0.44334 nm and the composition $\sim NbC_{0.76}$. This peak is shifted towards shorter interplanar spacings d relative to the narrow peak. The narrow peak corresponds to the coarse-crystalline fraction F_2 with a lattice constant of 0.44388 nm and the composition $\sim NbC_{0.79}$. The splitting into two peaks was observed for all structural reflections on the neutron diffraction patterns of all nanopowders. Thus, the detailed neutron diffraction study of NbC_y nanopowders revealed coexistence of two cubic fractions F_1 and F_2 of different composition, lattice constant (a_{B1}) and particle size.

A quantitative analysis of the neutron diffraction patterns of the nanopowders prepared by high-energy milling of carbide $NbC_{0.77}$, performed with allowance for experimental errors, showed that the lattice constants of the main (nanocrystalline) fraction F_1 and second (coarse-crystalline) fraction F_2 are ~ 0.4433 and ~ 0.4439 nm, respectively. The proportion of the F_1 fraction in the nanopowders prepared by milling for 5, 10 and 15 h was ~ 92, ~ 94 and $\sim 98\%$, respectively. The D_{CSR} values for the nanofractions of these nanocrystalline powders, determined from the broadening of the diffraction reflections, were ~ 35, ~ 17 and ~ 16 nm, respectively. The compositions of the nano- and coarse-crystalline fractions F_1 and F_2 evaluated [86] from the dependence of the lattice constant of disordered niobium carbide NbC_y on the content of carbon were $\sim NbC_{0.76}$ and $\sim NbC_{0.79}$, respectively. The particle size of the second fraction is 150 – 180 nm.

A SEM study[108] of of $NbC_{0.77}$ nanopowders confirmed inhomogeneous microstructure of their particles and revealed regions with different mutual orientations, interplanar spacings and lattice constants that could be associated with the fractions F_1 and F_2.

The average particle sizes of the nanocryslaline fraction F_1 in the nanopowders prepared by 5-, 10- and 15-h milling of carbide $NbC_{0.93}$ were ~ 47, ~ 45 and ~ 18 nm, respectively. The coarse-crystalline fraction F_2 is characterized by a nearly fixed composition $NbC_{0.95}$ and a particle size of about 200 nm. As the milling duration increases, the proportion of the nanocrystalline fraction F_1 increases, while that of the coarse-crystalline fraction F_2 decreases.

A decrease in the particle size of NbC_y powders from micro- to nano scale is accompanied by some increase in nonstoichiometry. For instance, the composition of carbide $NbC_{0.77}$ changed to $\sim NbC_{0.76}$ after milling for 5 and 10 h, while the composition of $NbC_{0.93}$ changed to $\sim NbC_{0.84}$, $\sim NbC_{0.82}$ and $\sim NbC_{0.80}$ after milling for 5, 10 and 15 h, respectively. As a result, it was found for the first time that the proportion of carbon in the niobium carbide nanoparticles prepared by milling and having a size of less than 50 nm decreases by 0.05 – 0.07 (5 – 8%) as compared to the initial carbide NbC_y. Such a large change in the composition leads to noticeable changes in the properties of the carbide, which should be taken into account in practice.

By and large, the results of studies of nanopowders of nonstoichiometric vanadium and niobium carbides show that a decrease in the size of carbide particles from micro- to nano scale is accompanied by changes in their composition with increasing nonstoichiometry with respect to carbon.

4. Nonstoichiometry of sulfides

The presence of structural vacancies in the non-metal or metal sublattice, which is characteristic of many coarse-crystalline sulfides, leads to noticeable deviations from stoichiometry. For instance, hexagonal iron sulfide with a NiAs-type structure contains structural vacancies in the iron sublattice and has a wide homogeneity range from $\sim Fe_{0.85}S$ to $\sim Fe_{0.93}S$.[10] High nonstoichiometry is characteristic of coarse-crystalline hexagonal and monoclinic copper disulfides whose composition varies from Cu_2S to $Cu_{1.96}S$, $Cu_{1.80}S$ and $Cu_{1.75}S$, as reported by different authors. Much larger deviations from stoichiometry were observed in Cu_xS ($x = 1.06 – 1.95$) thin films.[109] Cubic rare-earth metal sulfides MS_y (M = Ce, Nd, Ga, Tb) contain structural vacancies in the sulfur sublattice and have wide homogeneity ranges from $\sim MS_{0.75}$ to $MS_{1.00}$.[110] Cubic body-centred (β-$Ag_{2\pm\delta}S$) and face-centred (γ-$Ag_{2\pm\delta}S$) polymorphs of coarse-crystalline silver sulfide with $\delta = 0.001 – 0.02$ and even 0.3 are nonstoichiometric and both can be either silver-deficient or silver rich. Silver atoms in these polymorphs are randomly distributed over numerous crystallographic positions in the metal sublattice with probabilities that are much less than unity.[111, 112] It is these features of the crystal structure that are responsible for nonstoichiometry of cubic silver sulfides.

4.1. The structure and properties of nonstoichiometric nanoscale sulfides

Recently, there has been considerable interest in nanoscale semiconducting zinc, cadmium, mercury, lead, silver, tin and other metal sulfides.[25 – 28, 113 – 120] Transition of semiconducting sulfides from coarse-crystalline to nanocrystalline state is accompanied by not only a decrease in the particle (crystallite) size to nano scale, but also transformation of their electronic and optical properties due to the quantum size effects, as well as by changes in the crystal structure and by an increase in nonstoichiometry. For

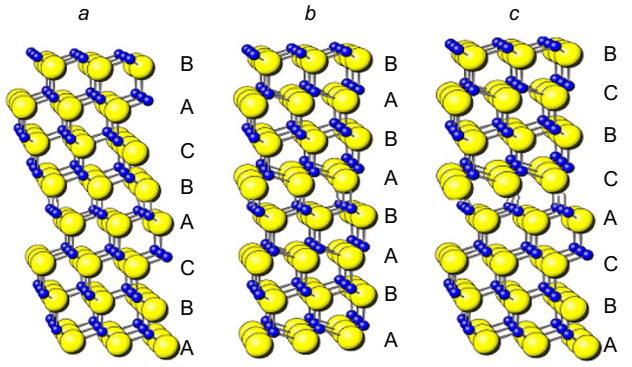


Figure 14. Stacking sequence of close-packed atomic planes in ordered and disordered phases of CdS:[124] *B*3-type cubic sphalerite structure (*a*); *B*4-type hexagonal wurtzite structure (*b*); and disordered nanocrystalline CdS (*c*).

instance, a decrease in the Cu_2S particle size to the nano scale causes a shift of the optical absorption peak owing to an increase in nonstoichiometry in the copper sublattice and to a change in the composition to $Cu_{2-x}S$.[121] Coarse-crystalline sulfide CdS has a hexagonal wurtzite (*B*4-type) structure[122] or a cubic sphalerite (*B*3-type) structure.[123] However, thin films, nano- and ultradisperse cadmium sulfide powders have a specific crystal structure that differs from the wurtzite and sphalerite structure. Thorough structural studies and simulation of cadmium sulfide nanoparticles[124, 125] revealed violation of periodic alternation of uniform close-packed atomic layers in CdS nanoparticles, so a specific disordered structure with randomly alternating close-packed hexagonal atomic planes is observed (Fig. 14).

The growth of stoichiometric CdS crystals requires an excess of sulfur since oxygen and sulfur form a volatile compound SO_2 with ease. The stoichiometric composition is characterized by the lowest concentration of intrinsic point defects ($\leqslant 5\times10^{16}$ cm^{-3}). All the optical, electrical and photoelectrical properties of CdS are determined by intrinsic point defects.

Of considerable interest is the dependence of the intensity and position of the exciton band in the cathodoluminescence spectrum on the method of preparation of CdS[126] and, therefore, on the main type of structural defects. Depending on stoichiometry, one or two bands appear in the luminescence spectra. The S : Cd ratio specifies the formation conditions and stability of edge-luminescence centres. The intensities of all luminescence bands in the spectra of single crystals depend on the proper defect structure. A thorough analysis of the growth conditions of stoichiometric crystals and types of intrinsic defects showed that the samples of nearly stoichiometric composition have a perfect structure, exhibit no misorientation for crystallite coalescence and represent mosaic single crystals with uniform structure. Crystal growth in the presence of excess sulfur leads to pronounced misorientation of blocks and to a decrease in the block size. An increase in the content of sulfur destabilizes crystals that undergo secondary transformations. In this case, the characteristic structural defect is a neutral vacancy in the cadmium sublattice (V_{Cd}). Cadmium-rich crystals contain a large amount of oxygen and an increase in layered heterogeneity is observed. The main type of structural defects is Cd_i^+. Crystal growth from the vapour phase in all cases occurs in the presence of oxygen, which replaces sulfur ions and serves as electron density acceptor. The presence of oxygen causes additional absorption in the low-energy region compared to the absorption edge. A complex pattern of cathodoluminescence spectra is due to inhomogeneity of the oxygen-containing crystals.

Luminescence is one of the most interesting properties of CdS nanoparticles. The dependence of the luminescence region on the nanoparticle size is explained by the size confinement and has been thoroughly studied.[17, 23, 127 – 129] Published data on the effect of nonstoichiometry are contradictory. The luminescence spectra of CdS nanoparticles less than 3.5 nm in size obtained in the strong confinement regime are to a great extent determined by impurity transitions.[130] Both shallow and deep energy levels within the band gap of CdS nanoparticles are due to intrinsic lattice defects or nonstoichiometry; such levels are formed by vacancies and interstitial atoms. Nonstoichiometry immediately affects the region and intensity of the luminescence of CdS nanoparticles. It was reported[131] that a deficiency of S^{2-} ions causes a decrease in the luminescence intensity. An excess of Cd^{2+} cations leads to an increase in the quantum yield, while an excess of S^{2-} anions causes this parameter to decrease.[132] Peaks at 557 and 563 nm in the fluorescence spectra of colloidal solutions (Fig. 15) are associated with vacancies in the cadmium sublattice.[133]

The intensity of the band with a maximum at 630 nm in the luminescence spectrum of poly(ethylene oxide)/CdS nanocomposites increased upon introducing excess Cd^{2+} ions and increasing the concentration of sulfur surface vacancies (V_S).[134] The introduction of excess sulfur ions led to a decrease in the intensity of this band down to disappearance and to a shift of luminescence towards the short-wavelength region.

By and large, it should be noted that a deviation from stoichiometry causes an increase in the probability of nonradiative decay of the excitation, which has an adverse effect on luminescence and can lead to concentration quenching of luminescence of colloidal solutions through migration-accelerated self-quenching by the hopping mechanism.[135]

Establishment of correlations between the method of synthesis of CdS nanoparticles, their nonstoichiometry and the formation of impurity levels and the optical properties is of interest for not only basic research, but also practice.[136] Solution to this problem can offer the possibility to extend the application fields of this optical material owing to targeted synthesis.

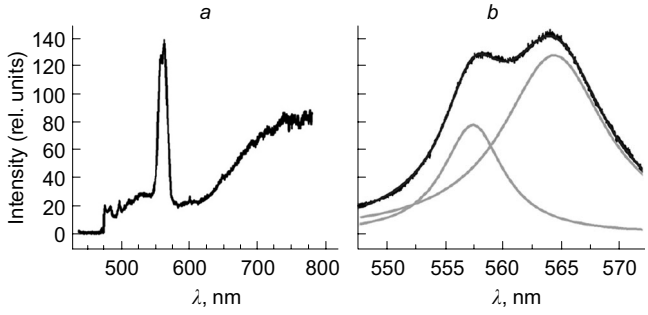


Figure 15. Fluorescence spectra of CdS nanoparticles:[133] general spectral pattern (*a*) and approximation of close-lying peaks by the sum of two Lorentzian curves (*b*). The excitation wavelength is 472.8 nm. This figure is provided courtesy of Springer Nature.

The appearance of intra-band electron energy levels associated with intrinsic defects occurs in different manner depending on the method of synthesis and matrix.[137] The material of the matrix used to fabricate nanoparticles significantly influences the stoichiometry of nanoparticles as well as the type and concentration of structural defects. In addition, the matrix layer near the surface of just-fabricated nanoparticles can act as a donor or acceptor of charge carriers, which can change the concentration of electrons on the surface of nanoparticles. This creates a potential difference between the surface and the bulk and causes changes in the charge carrier distribution inside the semiconductor. A thorough study[138] of the optical properties of CdS nanoparticles formed in different dielectric matrices showed that the main point defects in CdS nanoparticles in tetraethyl orthosilicate are I_S,† V_{Cd} and V_S. They make the major contribution to luminescence of CdS nanoparticles in the model liquid-glass matrix. Cadmium sulfide nanoparticles prepared by high-temperature synthesis mainly contain V_{Cd} and I_S point defects. The use of high-precision methods including small-angle X-ray scattering made it possible to study the dynamics of formation of CdS nanoparticles on heating. It was established that seeding and growth of the semiconductor phase occur throughout the temperature range studied rather than in the initial stage of the secondary heat treatment. As the particle size becomes equal to 19 nm, CdS nanoparticles adopt a hexagonal structure and contribute to photoluminescence in the emission region of the coarse-crystalline material.[139]

The results of structural studies of lead sulfide films are also ambiguous. It is assumed that PbS films have the same cubic (space group $Fm\bar{3}m$) $B1$-type structure[140] as the coarse-grained or single-crystalline samples. However, it was conjectured[141] that films contain cubic (space group $F\bar{4}3m$) nonstoichiometric sulfide $PbS_{0.90}$ with a $B3$-type structure. This was not confirmed in a study[14] of chemically deposited PbS thin films. More recently,[143] a thorough analysis of the results[141] and *in situ* studies of nanocrystalline PbS films (see Refs 143 – 145) showed that the films do have a cubic structure while do not belong to the $B3$ type. It was established[143–145] that sulfur atoms in the structure of nanocrystalline lead sulfide films are randomly distributed over two types of crystallographic positons, *viz*., octahedral 4(*b*) and tetrahedral 8(*c*). Cubic symmetry and the occupancies of the 4(*b*) and 8(*c*) positions by sulfur atoms, which differ from unity, suggest that the lead sulfide nanofilms have a $D0_3$-type crystal structure. Taking account of this fact, the chemical formula of lead sulfide in the nanofilms is $PbS^{(b)}_{0.84}S^{(c)}_{0.16}$ (see Ref. 145). Thus, PbS nanofilms demonstrate hidden nonstoichiometry in the sulfur sublattice.

Among methods of synthesis of nanocrystalline sulfide powders, films and nanoparticles, chemical deposition from aqueous solutions is most widely used. This technique is also termed chemical condensation, one-pot synthesis or hydrochemical deposition.

Hydrochemical deposition was for the first time performed in the synthesis of lead sulfide films in 1869.[146] Since then it has been used for the synthesis of various sulfides. The term chemical deposition for the first time appeared in a review[147] in which the first classification of different methods for the synthesis of sulfides was proposed. The history of the method of hydrochemical deposition of sulfide films and structures and modern trends in the field have been documented.[148]

4.2. Nonstoichiometry of nanostructured silver sulfide

Studies whose authors explicitly or indirectly observed the effect of the size of sulfide nanoparticles on changes in their composition and the occurrence of nonstoichiometry are of considerable interest. They were carried out taking nanostructured silver sulfide as an example.

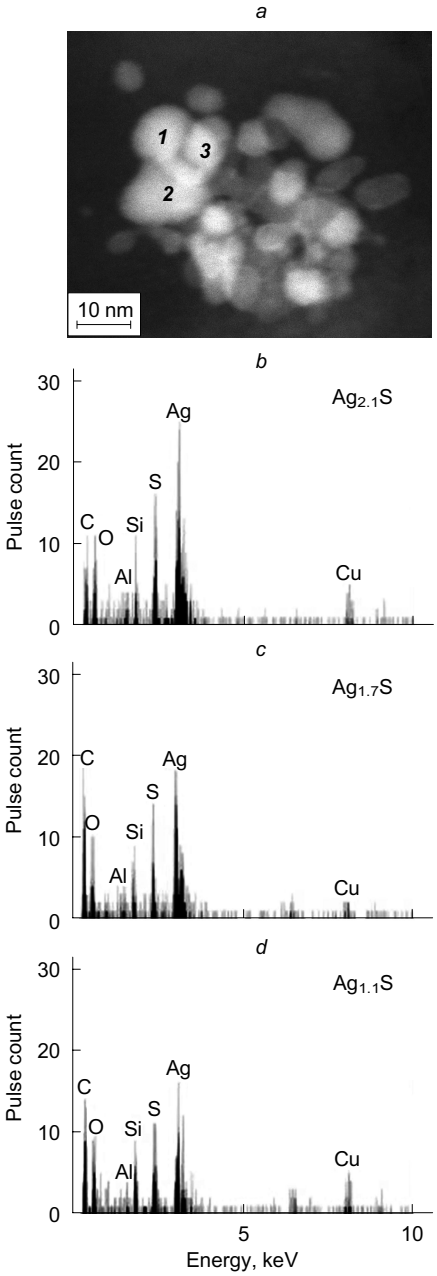


Figure 16. SEM image of an aggregate of silver sulfide nanoparticles (*a*) of size 16 (*1*), 10 (*2*) and 6 nm (*3*) and the corresponding EDX spectra (*b*–*d*).[149] According to EDX data, the chemical compositions are as follows: $Ag_{2.1}S$ ($Ag_2S_{0.95}$) for nanoparticle (*1*), $Ag_{1.7}S$ ($Ag_2S_{1.18}$) for nanoparticle (*2*) and $Ag_{1.1}S$ ($Ag_2S_{1.82}$) for nanoparticle (*3*). This figure is provided courtesy of American Chemical Society.

† I_S stands for interstitial sulfur.

Data on nonstoichiometry of nanostructured monoclinic (space group $P2_1/c$) acanthite are scarce. The EDX spectra were used [149] to determine the integrated intensities of the Ag*L* and S*K* lines of silver sulfide nanoparticles from 5 to 30 nm in size. The Ag : S atomic ratio was 2.1, 1.7 and 1.1 for nanoparticles ~16, ~10, and ~6 nm in size, respectively (Fig. 16). Thus, as silver sulfide nanoparticle size decreased from 16 to 6 nm their chemical composition changed from $Ag_{2.1}S$ ($Ag_2S_{0.95}$) to $Ag_{1.7}S$ ($Ag_2S_{1.18}$) and $Ag_{1.1}S$ ($Ag_2S_{1.82}$). The experimentally determined interplanar spacing d was 0.348 nm in all nanoparticles. This value is close to the interplanar spacing d_{020} = 0.346 nm in the monoclinic acanthite α-Ag_2S. In addition, a series of the [100] fast Fourier transform electron diffraction patterns calculated [149] from the TEM images of silver sulfide nanoparticles demonstrated a set of reflections from monoclinic (space group $P2_1/n$ or $P2_1/c$) acanthite and a number of unidentified reflections.

The Ag : S atomic ratio in 17-nm monoclinic $Ag_2S@SiO_2$ core – shell nanoparticles (Fig. 17) was 1.9 : 1.[150] This corresponds to nonstoichiometric sulfide $Ag_{1.9}S$ with vacancies in the metal sublattice.

The effect of the synthesis conditions on the crystal structure and possible deviation of the composition from stoichiometry was studied [151, 152] in relation to silver sulfide nanopowders with an average particle size of ⩽45 – 50 nm. Researchers from that group preliminarily determined the synthesis conditions and the crystal structure of coarse-crystalline silver sulfide powders (particle size from 515 ± 15 to 975 ± 15 nm).[153] It was found that coarse-crystalline silver sulfide has the stoichiometric composition Ag_2S and monoclinic (space group $P2_1/c$) acanthite-type structure. It was assumed [151, 152] that the nanopowder also has the stoichiometric composition and the same monoclinic structure as coarse-crystalline silver sulfide. A quantitative analysis of convergence of the calculated X-ray diffraction pattern obtained in this approximation with the experimental X-ray diffraction pattern of the nanopowder revealed poorer Rietveld parameters. Minimization of the experimental X-ray diffraction patterns with variation of the occupancy of crystallographic positions by silver and sulfur atoms significantly improved the convergence and the Rietveld agreement factors.

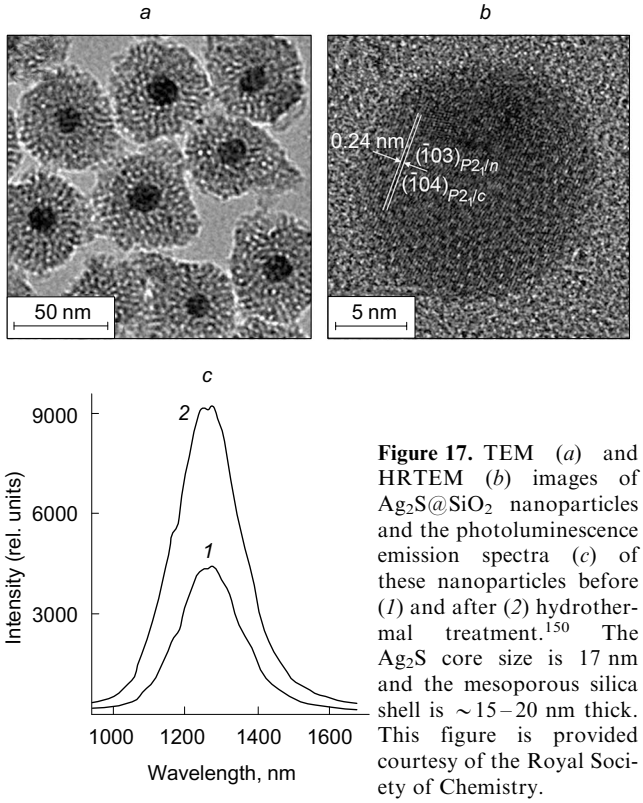


Figure 17. TEM (*a*) and HRTEM (*b*) images of $Ag_2S@SiO_2$ nanoparticles and the photoluminescence emission spectra (*c*) of these nanoparticles before (*1*) and after (*2*) hydrothermal treatment.[150] The Ag_2S core size is 17 nm and the mesoporous silica shell is ~15 – 20 nm thick. This figure is provided courtesy of the Royal Society of Chemistry.

Table 2. Refined crystal structure of monoclinic (space group $P2_1/c$) $Ag_{1.93}S$ nanocrystalline powder with acanthite-type structure (particle size is ~45 nm).[151]

Atom	Positon and multiplicity	Atomic coordinates			Occupancy	$B_{iso} \times 10^{-4}$, pm^2
		x/*a*	*y*/*b*	*z*/*c*		
Ag1	4(*e*)	0.0715	0.0151(0)	0.3093(9)	0.97	10.05(5)
Ag2	4(*e*)	0.7264	0.3240(9)	0.4375(0)	0.96	7.44(6)
S	4(*e*)	0.4920	0.2339(8)	0.1321(1)	1.00	1.960

Note. The lattice constants are as follows: a = 0.4234(3) nm, b = 0.6949(3) nm, c = 0.9549(5) nm, β = 125.43(6)°; the number of formula units in the unit cell is Z = 4; B_{iso} is the isotropic atomic displacement.

The lattice constants of α-Ag_2S nanopowder and the atomic coordinates of silver and sulfur (Table 2) are close to those of coarse-crystalline Ag_2S.[151, 152] However, the occupancies of the 4(*e*) position by the Ag1 and Ag2 atoms appeared to be lower than unity (~0.97 and ~0.96, respectively, see Table 2). Hence silver sulfide nanoparticles less than ~50 nm in size have the composition ~$Ag_{1.93}S$ and contain vacancies in the silver sublattice, thus being nonstoichiometric.

The acanthite – argentite phase transition and the structure of nanocrystalline acanthite and argentite were studied *in situ* by electron microscopy and X-ray diffraction in the temperature range of 300 – 503 K.[154 – 157] According to the X-ray diffraction data, at T < 433 K nanocrystalline silver sulfide has monoclinic (space group $P2_1/c$) acanthite-type structure and the composition ~$Ag_{1.93}S$ (Fig. 18 *a*); thus, this is a nonstoichiometric compound, which agrees with the results.[151] The average D_{CSR} parameter found from the broadening of the non-overlapping diffraction reflections ($\bar{1}02$), (110), ($\bar{1}13$), ($\bar{1}04$), (031) and (014) from monoclinic sulfide is ~40 nm. The acanthite – argentite phase transition is reversible and occurs at ~449 – 450 K.[154, 155]

The crystal structure of the high-temperature phase of silver sulfide (argentite) was determined using the X-ray diffraction patterns collected at 463 (Fig. 18 *b*) and 503 K. Structure refinement showed that at T > 433 K, silver sulfide contains only the cubic (space group $Im\bar{3}m$) phase with the structure of argentite β-Ag_2S. According to calculations, silver atoms in the structure are randomly distributed over the 6(*b*) and 48(*j*) positions (Table 3). The average D_{CSR} value for nanocrystalline cubic silver sulfide is ~50 and ~60 – 70 nm at 483 and 503 K, respectively.

The formation of argentite was confirmed by HRTEM.[154] The HRTEM images of silver sulfide nanopowder before and after heating above the acanthite – argentite transition temperature are shown in Fig. 19. The experimentally observed interplanar spacing of 0.309 nm is equal to the distance, $d_{(110)}$, between the (110) atomic planes in silver sulfide with the monoclinic (space group $P2_1/c$)

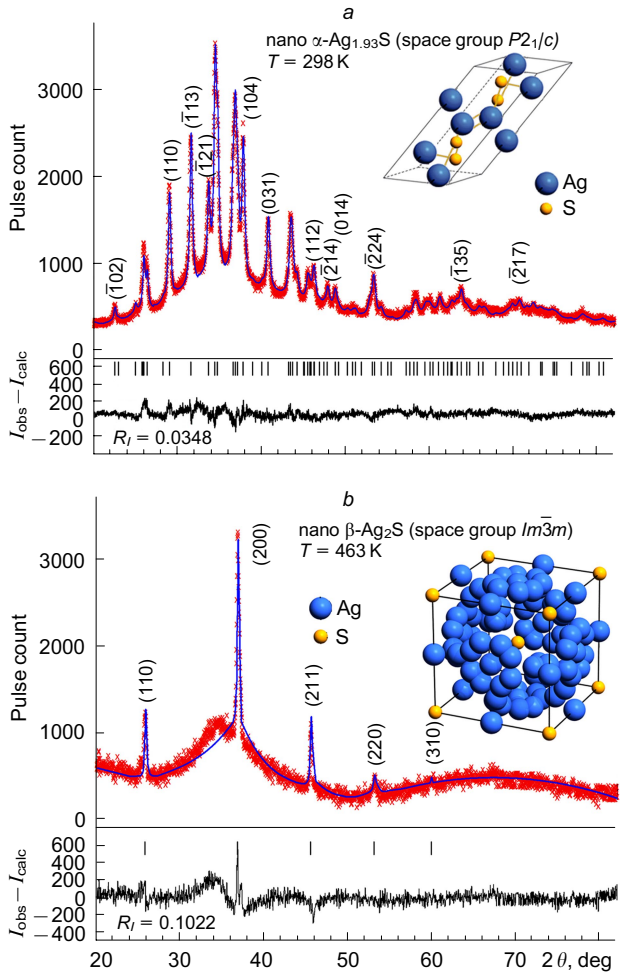


Figure 18. X-Ray diffraction patterns of nanocrystalline silver sulfide at room temperature (*a*) and at 463 K (*b*).[154, 155] Inset *a*: the unit cell of acanthite. Inset *b*: the unit cell of argentite. $I_{obs} - I_{calc}$ is the difference between the observed and calculated intensity (arb. units), R_I is the Rietveld agreement factor. Vertical bars mark positions of diffraction reflections. This figure is provided courtesy of PCCP Owner Societies.

Table 3. Atomic coordinates in cubic (space group $Im\bar{3}m$) argentite β-$Ag_{2.01}S$ at 503 K.[154, 155]

Atom	Positon and multiplicity	Atomic coordinates			Occupancy	$B_{iso} \times 10^{-4}$, pm^2
		x	*y*	*z*		
Ag1	6(*b*)	0	0.5	0.5	0.0978(7)	0.50
Ag2	48(*j*)	0	0.3306(5)	0.4122(7)	0.0711(0)	0.50
S	2(*a*)	0	0	0	1.00(0)	0.50

Note. The lattice constants are as follows: $a = b = c = 0.4874(1)$ nm, the number of formula units in the unit cell is $Z = 2$.

acanthite-type structure (Fig. 19 *a*). Heating of the nanopowder causes the acanthite–argentite phase transition, and the high-temperature phase is characterized by an interplanar spacing of 0.245 nm (Fig. 19 *b*) corresponding to the separation between the (200) atomic planes in cubic (space group $Im\bar{3}m$) argentite.

The occupancies of the 6(*b*) and 48(*j*) positions by the Ag1 and Ag2 silver atoms in argentite are very low, ~0.098 and ~0.071, respectively (see Table 3). The structure with

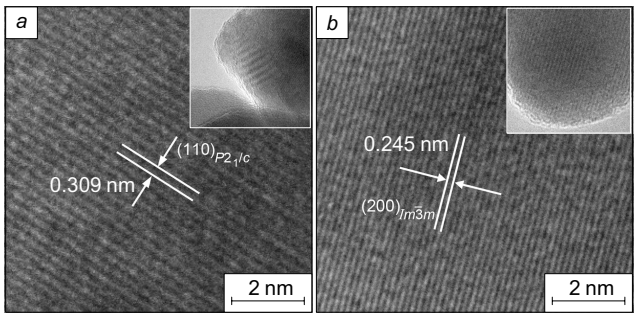


Figure 19. HRTEM images of silver sulfide nanoparticles of different structure.[154] Panel *a*: the interplanar spacing 0.309 nm observed before heating of nanoparticles corresponds to the $d_{(110)}$ distance in monoclinic silver sulfide (space group $P2_1/c$) with the acanthite structure; panel *b*: the interplanar spacing 0.245 nm observed after heating above the acanthite–argentite transition temperature corresponds to the $d_{(200)}$ distance in cubic silver sulfide (space group $Im\bar{3}m$) with the argentite structure. The insets demonstrate the TEM images of silver sulfide nanoparticles at smaller magnification. This figure is provided courtesy of PCCP Owner Societies.

so low occupancies of lattice sites is either unstable, which contradicts numerous experimental results, or stable owing to very high mobility of silver atoms (ions).

Argentite β-Ag_2S is a superionic conductor since the concentration of Ag^+ ions is much lower than the number of sites in the cationic sublattice. It is high positional disorder of Ag^+ ions and an ultrahigh concentration of vacancies in the silver sublattice (more than 92%) that facilitate diffusion of silver atoms in argentite by the vacancy mechanism, according to which a silver atom(ion) hops from an occupied site to adjacent vacancy site. In this case the metal sublattice in argentite can be treated as anisotropic Coulomb liquid of Ag^+ cations that diffuse in the effective potential of the body-centred cubic sulfur sublattice.

The shortest distances between the 48(*j*) sites in the argentite structure vary from 0.0561 to 0.2504 nm; therefore, occupation of a site by an Ag^+ ion excludes occupation of the nearest neighbour sites (from the first to the thirteenth coordination sphere) by another silver ion. If a silver ion occupies the 48(*j*) site, another silver ion can occupy the 48(*j*) site separated by a distance of at least 0.2511 nm, which corresponds to the fourteenth coordination sphere. The probability of this event is very low (~0.005). A more realistic situation is that one silver ion occupies the 6(*b*) site while the other one occupies the 48(*j*) site, thus being located in the fourth or fifth coordination sphere relative to the former ion.

Summing up, recent studies demonstrated that nanocrystalline silver sulfide with nanoparticles ~50 nm in size is nonstoichiometric in the temperature ranges where monoclinic acanthite and cubic argentite exist. Nonstoichiometry of acanthite nanoparticles is due to silver deficiency in the metal sublattice, while that of argentite nanoparticles is due to random distribution of only four silver atoms over 54 sites in the metal sublattice.

Mobility of Ag^+ ions in Ag_2S nanoparticles depends on external conditions, which enables the formation of hybrid structures,[158] changes in stoichiometry and subsequent formation of silver nanoparticles. It was established[159] that application of an electrical voltage to the

Ag_2S samples causes protrusion of silver on the Ag_2S surface.[159] The action of an electron beam on the $(Ag_2S)_x(Ag)_y$ heteronanostructure allows one to vary the $x : y$ ratio of sulfide to silver.[160] Changes in stoichiometry of silver sulfide nanoparticles up to formation of the Ag_2S/Ag hybrid structure can lead to coupling between semiconductor excitons and surface metal plasmons.[161 – 163] The formation of Ag_2S/Ag hybrid nanoparticles was detected upon ageing of sodium citrate-stabilized Ag_2S colloidal solutions under irradiation with light. Exposure of agglomerated Ag_2S nanoparticles deposited from a colloidal solution to an electron beam inside the column of the scanning electron microscope led to reversible growth of silver threads at the periphery of the Ag_2S nanoparticles (Fig. 20).[164]

Ag_2S nanoparticles have interesting luminescent properties; however, published data on the luminescence range are contradictory. Biological applications of Ag_2S quantum dots are based on their IR luminescence.[164 – 166] However, luminescence of Ag_2S nanoparticles in the visible region was also reported.[165, 167 – 169] Many results on the luminescence of Ag_2S in the visible region were obtained using nonstoichiometric hybrid Ag_2S/Ag nanoparticles and clusters surrounded by organic shells.[168, 170] One can assume that the shift of the luminescence range to the visible region is due to not only the presence of organic shell, but also nonstoichiometry of the Ag_2S nanoparticles. A study of the structure of Ag_2S nanoclusters stabilized in butyl thiolate showed that the $Ag_{14}S_{13}$ clusters are surrounded by S^{2-} ligands. The $Ag_{14}S_{13}$ core is further connected to the $[Ag(_{48}(SBu^t)_{32}]$ shell through Ag – S bonds and interactions between silver atoms.[170] The complex cluster emits bright red luminescence both in the solid state and in solution at room temperature. Possible stable clusters $(AgS)_n$ and their vibrational modes were also modelled theoretically.[171]

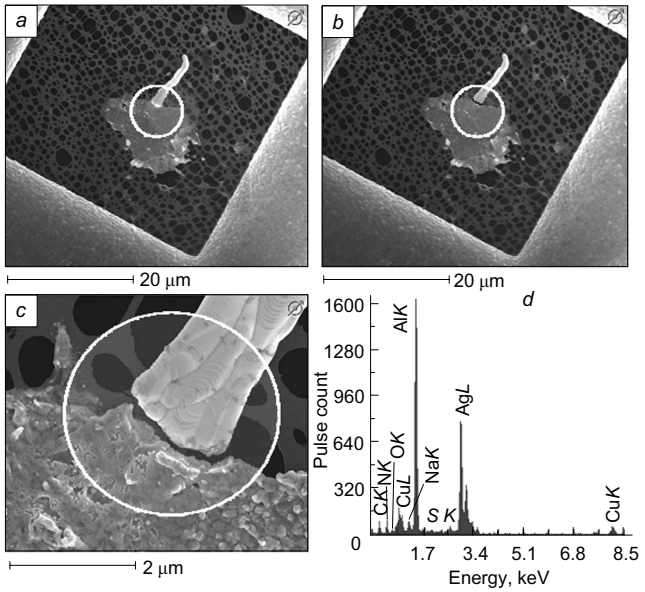


Figure 20. Photomicrographs illustrating the growth of a silver thread from Ag_2S nanoparticles under the action of electron beam.[164] The agglomerate of Ag_2S nanoparticles (*a*), silver thread separated from the Ag_2S agglomerate (*b*), the thread separation site (*c*), and the EDX spectrum of the thread (*d*). This figure is provided courtesy of Springer Nature.

Luminescence of nonstoichiometric silver sulfide nanoparticles in the visible region allows them to be used as fluorescent labels not only in the IR, but also in the visible region. A study on the effect of the size and charge of nonstoichiometric Ag_2S nanoparticles synthesized using different precursors on their interaction with red blood cells was reported.[172] It was found that the stabilizing shell significantly influences the result of the interaction, but no fluorescence of the conjugates in the visible region was observed.

The topicality of research into the stoichiometry and optical properties of Ag_2S nanoparticles is due to their antibacterial and photocatalytic properties. Hybrid porous Ag_2S/Ag nanoparticles demonstrate high photocatalytic activity in the visible region.[170] It was shown [173] that not only silver nanoparticles, but also zeolite-stabilized Ag_2S (acanthite) nanoparticles exhibit antibacterial activity, thus being promising for biomedical applications.

Different kinds of nanostructured silver sulfide are fabricated by thermal decomposition of organometallic precursors in hot solvents,[174, 175] by chemical vapour deposition of organometallic compounds,[176] by solvothermal,[177, 178] hydrothermal,[179, 180] mixed hydro(solvo)thermal,[181, 182] biomimetic,[183, 184] template, sol – gel, sonochemical, electrochemical and microwave-assisted methods,[116] by synthesis in microemulsions and by electron-beam etching.[185] Unfortunately, most of these methods afford only one form of nanostructured silver sulfide, *i.e.*, quantum dots, or nanopowders, or films, or heteronanostructures. Common drawbacks of many methods include the lack of control of the nanoparticle size during the synthesis, a broad nonuniform particle size distribution in the nanomaterials, multistaginess, the need to use sophisticated equipment, special protective equipment, elevated temperatures, and rare expensive and toxic reactants.

Chemical deposition from aqueous solutions[27, 28, 115, 116] is the most widely used and versatile method of synthesis of all modifications of nanostructured silver sulfide. In this case one can prepare coarse- and nanocrystalline powders, colloidal solutions of nanoparticles, isolated Ag_2S nanoparticles coated with a protective shell and various heteronanostructures based on Ag_2S.[27, 186]

Hydrochemical deposition of nanostructured Ag_2S using aqueous solutions of $AgNO_3$ and Na_2S in the presence of sodium citrate $Na_3C_6H_5O_7$ (Na_3Cit)[187] can serve as an example of the 'green chemistry' approach, which reduces or eliminates the use and generation of hazardous substances.[188] 'Green' synthesis of stable, monodisperse and nontoxic Ag_2S nanoparticles is also performed in aqueous solutions of $AgNO_3$ and Na_2S using (3-sulfanylpropyl)trimethoxysilane as stabilizer.[189, 190]

Owing to the small solubility product K_{sp} ($K_{sp,Ag2S} = 6.3 \times 10^{-50}$ at 298 K, see Ref. 191) Ag_2S is deposited from aqueous solutions of $AgNO_3$ and Na_2S following the simple reaction

$$2\,AgNO_3 + Na_2S = Ag_2S\downarrow + 2\,NaNO_3 \qquad (3)$$

The concentrations, $C_{S^{2-}}$ and C_{Ag^+}, of the S^{2-} and Ag^+ ions, respectively, in the ideal process (3) are interrelated

$$C_{S^{2-}} = \frac{C_{Ag^+}}{2}. \quad (4)$$

Small changes in the reactant concentration ratio $C_{Ag^+}/C_{S^{2-}}$ compared to reaction (3), the use of complex-forming agents and stabilizers as well as control of the synthesis conditions allow one to synthesize coarse- and nanocrystalline powders, colloidal nanoparticles, core–shell particles and other types of nanostructured silver sulfide.

Deposition of silver sulfide in the presence of Na_3Cit as stabilizer proceeds in a neutral medium at pH ~ 7 by the following reaction scheme:

$$2\,AgNO_3 + (1 \pm \delta)\,Na_2S \xrightarrow{NaCit} Ag_2S\downarrow + 2\,NaNO_3 \quad (5)$$

where $\delta \geqslant 0$.

Silver sulfide nanopowders with an average particle size of less than 60 nm are prepared by deposition from aqueous $AgNO_3$ and Na_2S solutions with concentrations 50 mmol L^{-1} and $C_{Na_2S} = C_{AgNO_3}/2 + \delta$, where $\delta = 0.5$ mmol L^{-1}, in the presence of Na_3Cit in the dark.[151, 186, 187, 192] A small excess of sodium sulfide is necessary for the synthesis of silver sulfide containing no metallic silver impurity.

Stable colloidal solutions of silver sulfide with nanoparticles from 2 to 16 nm in size are synthesized from aqueous reaction mixtures with $AgNO_3$ concentrations from 0.3125 to 2.5 mmol L^{-1}, $C_{Na_2S} = C_{AgNO_3}/2 + \delta$, where $\delta = 0.01$ mmol L^{-1}, and a Na_3Cit concentration ranging from 1 to 15 mmol L^{-1} in the dark.[186, 193] A small excess of sodium sulfide favours the preparation of colloidal solutions of silver sulfide containing no silver nanoparticles.

The electronic and optical properties of semiconducting silver sulfide nanoparticles are modified by the synthesis of hybrid core–shell heteronanostructures, *e.g.*, $Ag_2O@Ag_2S$.[194] Hydrochemical deposition of heteronanostructures also allows one to create a protective shell on the surface of semiconductor nanoparticles.

Core–shell nanoparticles with a silver sulfide core and a carbon-containing citrate shell were synthesized in aqueous reaction mixtures of $AgNO_3$ and Na_2S containing different amounts of Na_3Cit.[195, 196] The formation of the shell and the shell thickness depend on the concentration ratio of the silver and sulfur precursors, on the one hand, and on the sodium citrate concentration, on the other hand. It was shown[186, 195, 196] that a continuous shell surrounding the Ag_2S cores is formed if $C_{Ag^+}/4 \leqslant C_{Cit^{3-}} \leqslant C_{Ag^+}$. By varying the initial reactant concentrations and the deposition conditions one can synthesize $Ag_2S@C$ nanoparticles with a core size ranging from 10 to 50 nm and a non-toxic carbon-containing citrate shell from 1.5 to 10 nm thick.

Nanocomposites, *e.g.*, Ag_2S/Ag heteronanostructures are fabricated by different methods from cation exchange to sulfidization of nanoparticles and thin films and laser ablation.[197–201] Most of these methods are complicated and difficult to implement. It was reported[202–206] that Ag_2S/Ag heteronanostructures can be deposited upon irradiation of aqueous solutions of $AgNO_3$, Na_2S and Na_3Cit with reduced concentration of sodium sulfide $C_{Na_2S} < C_{AgNO_3}/2$. In this case, sulfide Ag_2S is formed simultaneously with silver nanoparticles that are formed owing to photochemical reduction of Ag^+ ions with citrate ions $C_6H_5O_7^{3-}$. Coalescence of Ag and Ag_2S nanoparticles produces Ag_2S/Ag nanocomposites.

The results presented above demonstrate that hydrochemical deposition is the most versatile method for the preparation of nanostructured silver sulfide. It allows one to synthesize all kinds of nanostructured silver sulfide with controlled particle size from the same nontoxic reactants by varying only their concentrations in solution and by carrying out the synthesis in the dark or in the light. Hydrochemical deposition of silver sulfide does not involve the use or generation of hazardous substances. The versatile method of chemical deposition from aqueous solutions can be used to synthesize all kinds of nanostructured sulfides of other metals (Cd, Zn, Pb and Cu) by replacing the silver salts with corresponding metal salts.

5. Note added in proof

Now we will briefly outline certain recent publications.

It was proposed[207] to use nonstoichiometric titanium oxide TiO_y with different content of oxygen in a $Pt/Al_2O_3/TiO_x/TiO_y/Ti/Pt$ device as current suppression layer to reduce the power consumption of resistive random access memory. Titanium oxide thin films were deposited by d.c. reactive sputtering of a titanium target with a fixed d.c. power at 150 W (300 V, 0.5 A) in an argon and oxygen atmosphere. Experiments showed that the additional TiO_y layer causes a decrease in the operating current and power consumption of the RRAM device since the TiO_y layer operates as a transistor, *i.e.*, current limiter. One more possible application is as follows. To be used as metal–oxide–semiconductor (MOS) capacitors and MOS field-effect transistors (MOSFETs), AlO_x/TiO_y thin films were grown on H-diamond by atomic layer deposition.[208] The oxide insulating films demonstrated a maximum capacitance density and ultrahigh dielectric constant. The effect of nonstoichiometry and degree of long-range order on the crystal structure of the monoxide TiO_y was studied by X-ray diffraction, Raman spectroscopy and electron microscopy.[209] It was found that nonstoichiometry in TiO_y affects the intensity of the peak associated with the vibrational mode of the Ti–O bond in the Raman spectra and on the composition of phases formed in the ordered TiO_y. A mechanism was proposed of precipitation of additional phases in the matrix with a cubic structure during heat treatment. It involves diffusion of vacancies in dislocations followed by their collapse upon accumulation, as well as the formation of open and closed pores. It was established that the direction of growth of new phases in TiO_y is specified by the matrix cubic phase. The motion of vacancies in dislocations is the main mechanism preceding the phase transitions with the formation of new phases including Ti_2O, Ti_2O_3 and an additional oxygen-rich phase.

Recently, there has been increasing interest in bioactive nanomaterials with calcium sulfate matrices.[210–215] Biocompatible nanoparticles added to such matrices impart them new functional properties. In this connection the intention to use 'green' synthesis is of great importance.[216–220] However, one should take account of the fact that even small amounts of additives or inserted atoms and ions can either improve or deteriorate the

properties of the final nanocomposite.[221, 222] A thorough study of the thermal behaviour of nanocomposites containing TiO_y nanoparticles of different stoichiometry ($TiO_{0.92}$ and $TiO_{1.23}$, 10 and 20 mass % in both cases) and 20 – 40 nm in size was reported.[223] An increase in temperature as a result of the interaction between the matrix and the introduced TiO_y nanoparticles used as an additive causes oxidation of titanium monoxide to titanium dioxide. A joint analysis of thermogravimetric, differential thermal, and powder X-ray diffraction data made it possible to determine the temperature ranges corresponding to the onset of changes in the valence state of titanium and to the phase transitions of the nanocomposites. The interaction of HAp and TiO_y additives, as components of nanocomposites, significantly changes the thermal behaviour of nanocomposites compared to that of unmodified HAp. The change in the valence state of Ti^{2+} ion to Ti^{3+} and Ti^{4+} begins at 623 K (350 °C) while T = 880 K (607 °C) corresponds to the maximum intensity of the formation of the $Ti_{4.5}O_5$ phase in the $TiO_{0.92}$ (20 mass %)/Hap nanocomposite. Thermal decomposition of nanocomposites occurs at much higher temperatures than that of the unmodified milled HAp. Both the matrix and additive nanoparticle sizes remain unchanged below the matrix degradation temperature. The newly formed β-tricalcium phosphate (TCP) is not nanocrystalline. The uptake of structural oxygen from HAp by titanium monoxide competes with the formation of β-TCP. Besides, TiO_y additives stabilize the matrix. The change in the amount of heat released in in exo- and endothermic reactions and the change in the mass on heating depend on the initial composition of the sample, *i.e.*, on the TiO_y stoichiometry and mass content. The maximum deviation of the temperature dependences of the observed changes compared to those of the unmodified HAp was found at a $TiO_{0.92}$ content of 20 mass %. The study showed that the design of novel nanomaterials should involve a comprehensive analysis of the interaction between the matrix and additives. Fine interactions between nanoparticles of these phases affect the properties of the matrix (defect formation, crystal structure, phase composition), while changes in the additive stoichiometry lead to changes in the properties of the final nanocomposite, which allows one to fabricate materials with specified properties.

New methods of computer simulation make it possible to predict the behaviour and mutual influence of components of nanomaterials.[224, 225]

A new method for the synthesis of nonstoichiometric carbide NbC_y by vacuum heat treatment of niobium citrate was proposed.[226] According to powder X-ray diffraction, SEM, TEM, and adsorption data, the nanopowder has a cubic structure (space group $Fm\bar{3}m$), isometric morphology, D_{CSR} ~12 nm and a specific surface area of ~211.9 $m^2\,g^{-1}$. An electrocatalyst based on nanocrystalline NbC_y is characterized by low hydrogen overvoltage (−245 mV) and high stability. Nonstoichiometric nanocrystalline NbC_y can thus be considered as promising electrode material for electrocatalytic production of hydrogen from renewable aqueous alcoholic solutions.

Nanocrystalline niobium and vanadium carbides prepared by high-energy milling[89] have inhomogeneous microstructure.[227] The sequence of ordering in highly nonstoichiometric niobium carbide, which is related to formation of Nb_6C_5 superstructures and grinding of the microstructure due to ordering, was studied theoretically.[228] The effect of anisotropy of the microstructure and nonstoichiometry of niobium carbide composition was studied for the first time.[105, 229]

The possibility to synthesize Ag_2S nanoparticles with different organic stabilizers can be used to study self-organization[230, 231] and to find new promising fields of application of nonstoichiometric silver sulfide nanoparticles.

It was shown[232, 233] that, chemically, aqueous solutions containing ultralow concentrations of reactants used for liquid-phase synthesis of silver sulfide nanoparticles represent supersaturated aqueous solutions with respect to the content of silver and sulfur ions. Liquid-phase synthesis of colloidal Ag_2S nanoparticles (quantum dots) for small-angle neutron scattering studies of the fine structure, size and shape of nanoparticles was for the first time carried out in heavy water D_2O.[234, 235] Additional studies on hydrochemical synthesis of nanocrystalline silver sulfide revealed the presence of star-like superhydrophobic particles of finely dispersed metallic silver[236, 237] with the relative density lower than the density of water. No information on such silver particles has been reported so far. The ultradisperse silver powder with star-like particles can potentially be used in microelectronics, catalysis, medicine and as superhydrophobic material for protective coatings.

Nanocrystalline Ag_2S powder and Ag_2S/Ag heteronanostructures demonstrate enhanced catalytic activity in reactions of photocatalytic hydrogen release from aqueous solutions in the presence of Na_2S and Na_2SO_3.[238, 239] The most intense hydrogen release was observed for the Ag_2S/Ag heteronanostructures composed of nonstoichiometric monoclinic sulfide $Ag_{1.93}S$ and metallic silver.

Additional investigations of the structure and thermal stability of the size and phase composition of semiconducting silver sulfide nanoparticles[240 – 243] demonstrated that the thermal stability of the size of Ag_2S nanoparticles is lower than that of the size of lead sulfide (PbS) nanoparticles.[244] Growth of silver sulfide nanoparticles begins at ~460 K (*cf.* ~700 K for lead sulfide nanoparticles). Probably, the narrower range of thermal stability of the size of Ag_2S nanoparticles is due to the lower melting point of silver sulfide. In addition, lead sulfide thin layers are characterized by short-range order and correlations in the mutual arrangement of sulfur atoms,[245] which also can influence the thermal stability of the composition and the nanoparticle size. There are a number of studies on the effect of temperature and keeping in air on the particle size and recrystallization of silver and lead sulfide nanopowders.[246 – 248]

Investigations of thermal expansion and heat capacity of nanocrystalline silver and lead sulfides and their solid solutions[247 – 253] made it possible to gain a better insight into effect of the nano state on these properties and to refine the numerical values of the enthalpies of phase transitions of silver sulfide in the temperature range of ~273 – 930 K. The elastic properties of coarse- and nanocrystalline cubic superionic silver sulfide[254, 255] with the argentite (β-Ag_2S) structure were determined experimentally and theoretically for the first time.

Any electronic properties and applications of silver sulfide (especially, in microelectronics) are related to the reversible acanthite αAg_2S – argentite β-Ag_2S transition occurring in the temperature range of ~448 – 453 K. Exper-

imental and theoretical studies [256 – 260] of (i) atomic displacements in the course of this transition and (ii) the phenomenon *per se* treated as two-sublattice ordering will allow one to extend the application fields of nanocrystalline silver sulfide.

6. Conclusion

Advancement of research into different-purpose nanostructured materials contributes to the scientific and technological progress. An important problem in studies of nanostructured compounds and materials is to determine how the size of nanoparticles influences their nonstoichiometry. In this review we considered the interplay between nonstoichiometry and size of nanoparticles taking two different types of compounds:

— Group IV – VI transition metal oxides and carbides, which are essentially nonstoichiometric compounds in the coarse-crystalline state; and

— semiconducting sulfides, which normally have stoichiometric compositions but become nonstoichiometric as their particle size decreases to the nano scale.

The first group of compounds can contain structural vacancies either in one or both (metal and nonmetal) sublattices. The proportion of vacancies can be as high as several tens of per cent. Nanostructured semiconducting sulfides are characterized by much lower nonstoichiometry, which usually is at most a few per cent.

Nanostructured oxides and carbides are mainly fabricated by high-energy milling. Thorough diffraction studies showed that a decrease in the particle size of nonstoichiometric oxides and (especially) carbides is accompanied by an increase in nonstoichiometry.

High-energy milling followed by annealing of titanium monoxide was used to prepare and stabilize the ordered orthorhombic nanophase Ti_9O_{10}. According to free-energy quantum chemical calculations for the Ti_9O_{10} microcrystalline phase and nanophase, only the latter is stable owing to specific features of its surface relaxation.

The ordered phase V_8C_7, which is stoichiometric in the coarse-crystalline state, changes its composition to $V_8C_{7-\delta}$ as the particle size becomes 30 – 40 nm and smaller, *i.e.*, its ordered carbon sublattice becomes nonstoichiometric.

The proportion of carbon in niobium carbide nanoparticles less than 50 nm in size prepared by milling decreases by 0.05 – 0.07 (5 – 8%) compared to the initial carbide NbC_y.

The occurrence of nonstoichiometry in sulfide nanoparticles synthesized in different manner is due to an increase in the proportion of surface atoms with decreasing particle size. Chemical bonds between surface atoms are weaker than those between atoms inside nanoparticles, which leads to nonstoichiometry.

Summing up, we for the first time established that the decrease in the particle size in fundamentally different solids (disordered and ordered carbides, oxides, sulfides) to 30 – 50 nm and smaller leads to noticeable increase or occurrence of nonstoichiometry. This experimental fact is of great importance for understanding the nature of the nanocrystalline state and the size effects that affect not only the physical properties (especially, in the case of semiconductors), but also the composition of solids as a result of increase in or occurrence of nonstoichiometry.

Research into nanocrystalline solids cannot be reduced to studies of the aspects related to the small particle size. The interplay between the particle size and nonstoichiometry found in the fundamentally different compounds (see above) suggests this is a common feature which should be taken into account in studies of all nanocrystalline solids.

By and large, our analysis of published data on nanocrystalline compounds revealed a strong correlation between the nanoparticle size and nonstoichiometry. It should be taken into account when performing the synthesis and studying the structure and properties of nanocrystalline solids and materials based on them.

This review was supported in part by the Russian Science Foundation (Project No. 14-23-00025). It was also supported within the framework of the State Assignment to the Institute of Solid State Chemistry, Ural Branch of the Russian Academy of Sciences, under Contract No. 0397-2019-0001.

7. List of acronyms

CSR — coherent scattering region,
d — interplanar spacing,
D_{CSR} — size of coherent scattering region,
EDX — energy dispersive X-ray spectroscopy,
E_g — energy band gap,
HAp — hydroxyapatite,
hkl — Miller indices,
HRFD — high-resolution Fourier diffractometer,
HRTEM — high-resolution transmission electron microscopy,
K_{sp} — solubility product,
SEM — scanning electron microscopy,
TEM — transmission electron microscopy,
TOF — time-of-flight.

References

1. J.L.Proust. *Ann. Chim. Phys.*, **32**, 26 (1799)
2. J.A.Dalton. *A New System of Chemical Philosophy*. Vol. 1, Pt 2. (Manchester, 1810)
3. J.B.Richter. *Anfangsgründen der Stöchiometrie: oder, Messkunst chemischer Elementen*. Bd. 1, 2. (Breslau, 1792 – 1794)
4. C.L.Bertholett. *Essai de Statique Chimique. Premiere Partie*. (Paris: Firmin Didot, 1803)
5. A.I.Gusev, A.A.Rempel. In *Bol'shaya Rossiiskaya Entsiklopediya*. (Big Russian Encyclopedia) Vol. 34. (Moscow: BRE, 2017). P. 75
6. A.A.Rempel, A.I.Gusev. *Nestekhiometriya v Tverdom Tele*. (Nonstoichiometry in Solids). (Moscow: Fizmatlit, 2018)
7. F.I.Gusev. In *Bol'shaya Rossiiskaya Entsiklopediya*. (Great Russian Encyclopedia) Vol. 22. (Moscow: BRE, 2013). P. 517
8. L.S.Darken, R.W.Gurry. *J. Am. Chem. Soc.*, **67**, 1398 (1945)
9. E.K.Kostyukhin, L.M.Kustov. *Mendeleev Commun.*, **28**, 559 (2018)
10. H.Krebs. *Grundzüge der Anorganischen Krisstallchemie*. (Stuttgart: Ferdinand Enke Verlag, 1968)
11. J.S.Anderson. In *The Chemistry of Extended Defects in Non-Metallic Solids*. (Eds L.Eyring, M.O'Keeffe). (Amsterdam; London: North-Holland Publishing, 1970). P. 1

12. J.S.Anderson. In *Modern Aspects of Solid State Chemistry*. (Ed. C.N.R.Rao). (New York: Plenum Press, 1970). P. 29
13. G.P.Shveikin, S.I.Alyamovskii, Yu.G.Zainulin, F.I.Gusev, V.A.Gubanov, E.Z.Kurmaev. *Soedineniya Peremrnnogo Sostava i Ikh Tverdye Rastvory*. (Compounds of Variable Composition and their Solid Solutions). (Sverdlovsk: Ural Scientific Centre, 1984)
14. A.I.Gusev. *Fizicheskaya Khimiya Nestekhiometricheskikh Tugoplavkikh Soedinenii*. (Physical Chemistry of Nonstoichiometric Refractory Compounds) (Moscow: Nauka, 1991)
15. A.I.Gusev, A.A.Rempel. *Nestekhiometriya, Besporyadok i Poryadok v Tverdom Tele*. (Nonstoichiometry, Disorder and Order in a Solid). (Ekaterinburg: Ural Branch, Russian Academy of Sciences, 2001)
16. A.I.Gusev. *Nestekhiometriya, Besporyadok, Blizhnii i Dal'nii Poryadok v Tverdom Tele*. (Nonstoichiometry, Disorder and Short-Range and Long-Range Order in a Solid). (Moscow: Fizmatlit, 2007)
17. A.P.Alivisatos. *Science*, **271**, 933 (1996)
18. A.P.Alivisatos. *J. Phys. Chem.*, **100**, 13226 (1996)
19. *Nanotechnology Research Directions*. (Eds M.C.Roco, R.S.Williams, P.Alivisatos). (Dordrecht: Kluwer Academic Publishing, 2000)
20. *Springer Handbook of Nanotechnology*. (Ed. B.Bhushan). (Heidelberg, Berlin: Springer, 2004)
21. A.A.Semenova, A.B.Tarasov, E.A.Gudilin. *Mendeleev Commun.*, **29**, 479 (2019)
22. A.I.Gusev, A.A.Rempel. *Nanocrystalline Materials*. (Cambridge: Cambridge International Science Publishing, 2004)
23. A.A.Rempel. *Russ. Chem. Rev.*, **76**, 435 (2007)
24. A.I.Gusev. *Nanomaterials, Nanostructures, Nanotechnology*. (3rd Edn.). (Nanomaterials, Nanostructures, Nanotechnologies). (Moscow: Fizmatlit, 2009)
25. H.-E.Schaefer. *Nanoscience. The Science of the Small in Physics, Engineering, Chemistry, Biology and Medicine*. (Heidelberg, Dordrecht, New York: Springer, 2010)
26. A.A.Rempel. *Russ. Chem. Bull., Int. Ed.*, **62**, 857 (2013)
27. S.I.Sadovnikov, A.A.Rempel, A.I.Gusev. *Nanostructured Lead, Cadmium and Silver Sulfides: Structure, Nonstoichiometry and Properties*. (Cham, Heidelberg: Springer International Publishing, 2018)
28. S.I.Sadovnikov, A.I.Gusev, A.A.Rempel. *Poluprovodnikovye Nanostruktury Sul'fidov Svintsa, Kadmiya i Serebra*. (Semiconductor Nanostructures of Lead, Cadmium and Silver Sulfides) (Moscow: Fizmatlit, 2018)
29. J.Murray, H.A.Wriedt. *Bull. Alloy Phase Diagr.*, **8**, 148 (1987)
30. H.Okamoto. *J. Phase Equilib. Diff.*, **32**, 473 (2011)
31. S.Anderson, B.Collen, U.Kuylenstierna, A.Magneli. *Acta Chem. Scand.*, **11**, 1641 (1957)
32. M.D.Banus, T.B.Reed. In *The Chemistry of Extended Defects in Non-Metallic Solids*. (Eds L.Eyring, M.O.Keeffe). (Amsterdam, London: North-Holland Publishing, 1970). P. 488
33. D.Watanabe, J.R.Castles, A.Jostson, A.S.Malin. *Nature (London)*, **210**, 934 (1966)
34. E.Hilti. *Naturwissenschaften*, **55**, 130 (1968)
35. A.I.Gusev, A.A.Valeeva. *JETP Lett.*, **96**, 364 (2012)
36. A.I.Gusev. *J. Solid State Chem.*, **199**, 181 (2013)
37. S.Amano, D.Bogdanovski, H.Yamane, M.Terauchi, R.Dronskowski. *Angew. Chem., Int. Ed.*, **55**, 1652 (2016)
38. B.V.Khaenko, E.T.Kachkovskaya. *Poroshkovaya Metallurgiya*, (6), 52 (1986)
39. A.A.Valeeva, A.A.Rempel, A.I.Gusev. *Inorg. Mater.*, **37**, 603 (2001)
40. A.A.Valeeva, A.A.Rempel, A.I.Gusev. *JETP Lett.*, **71**, 460 (2000)
41. A.A.Valeeva, S.Z.Nazarova, A.A.Rempel. *Phys. Solidi State*, **58**, 771 (2016)
42. A.A.Valeeva, S.Z.Nazarova, A.A.Rempel. *Phys. Status Solid B*, **253**, 392 (2016)
43. A.A.Valeeva, S.Z.Nazarova, A.A.Rempel. *JETP*, **122**, 722 (2016)
44. S.Bolokang, D.E.Motaung, C.J.Arendse, T.F.G.Muller. *Mater. Charact.*, **100**, 41 (2015)
45. I.Veljković, D.Poleti, M.Zdujić, L.Karanović, Č.Jovalekić. *Mater. Lett.*, **62**, 2769 (2008)
46. J.-L.He. *Adv. Powder Technol.*, **27**, 1868 (2016)
47. A.A.Valeeva, S.V.Rempel. *Bull. Russ. Acad. Sci.*: *Phys.*, **82**, 834 (2018)
48. A.A.Valeeva, K.A.Petrovykh, H.Schroettner, A.A.Rempel. *Inorg. Mater.*, **51**, 1132 (2015)
49. A.A.Valeeva, M.G.Kostenko. *Nanosystems: Phys., Chem., Mathem.*, **8**, 816 (2017)
50. A.A.Valeeva, M.G.Kostenko, S.Z.Nazarova, E.Yu.Gerasimov, A.A.Rempel. *Inorg. Mater.*, **54**, 568 (2018)
51. A.A.Valeeva, A.Pfizner, A.A.Rempel. *Monatsh. Chem.*, **146**, 1205 (2015)
52. M.G.Kostenko, A.A.Valeeva. *Mendeleev Commun.*, **29**, 405 (2019)
53. V.Jandova, Z.Bastl, J.Šubrt, J.Pola. *J. Anal. Appl. Pyrolysis*, **92**, 287 (2011)
54. J.Blazevska-Gilev, V.Jandova, J.Kupčik, Z.Bastl, J.Šubrt, P.Bezdička, J.Pola. *J. Solid State Chem.*, **197**, 337 (2013)
55. B.Pabon, J.Beltran, G.Sanchez-Santolino, I.Palacio, J.Lopez-Sanchez, J.Rubio-Zuazo, J.Rojo, P.Ferrer, A.Mascaraque, M.Munoz. *Nat. Commun.*, **6**, 6147 (2015)
56. J.Xu, D.Wang, H.Yao, K.Bu, J.Pan, J.He, F.Xu, Z.Hong, X.Chen, F.Huang. *Adv. Mater.*, **30**, 1706240 (2018)
57. A.K.Vasilevskaia, V.I.Popkov, A.A.Valeeva, A.A.Rempel. *Russ. J. Appl. Chem.*, **89**, 1211 (2016)
58. V.I.Popkov, A.K.Bachina, A.A.Valeeva, A.A.Lobinsky, E.Y.Gerasimov, A.A.Rempel. *Ceram. Int.*, **46**, 24483 (2020)
59. A.A.Rempel, A.A.Valeeva, A.S.Kurlov, G.Klinser, W.Sprengel. *Mendeleev Commun.*, **29**, 486 (2019)
60. I.S.Popov, A.N.Enyashin, A.A.Rempel. *Superlat. Microstr.*, **113**, 459 (2018)
61. M.E.Straumanis, H.W.Li. *Z. Anor. Allg. Chem.*, **305**, 143 (1960)
62. M.E.Straumanis, T.Ejima, W.J.James. *Acta Cryst.*, **14**, 493 (1961)
63. A.N.Golubenko, T.N.Rezukhina. *Izv. Akad. Nauk SSSR, Neorg. Mater.*, **3**, 101 (1967)
64. M.Zhang, G.Yao, Y.Cheng, Y.Xu, L.Yang, J.Lv, S.Shi, X.Jiang, G.He, P.Wang, X.Song, Z.Sun. *Appl. Surf. Sci.*, **356**, 546 (2015)
65. L.Li, J.Ya, F.Hu, Z.Liu, E.Lei. *J. Energy Chem.*, **25**, 740 (2016)
66. A.A.Valeeva, E.A.Kozlova, A.S.Vokhmintsev, R.V.Kamalov, I.B.Dorosheva, A.A.Saraev, I.A.Weinstein, A.A.Rempel. *Sci. Rep.*, **8**, 9607 (2018)

67. A.A.Valeeva, I.B.Dorosheva, E.A.Kozlova, R.V.Kamalov, A.S.Vokhmintsev, D.S.Selishchev, A.A.Saraev, E.Yu.Gerasimov, Weinstein, A.A.Rempel. *J. Alloys Compd.*, **796**, 293 (2019)
68. A.A.Rempel, A.A.Valeeva. *Russ. Chem. Bull., Int. Ed.*, **68**, 2163 (2019)
69. A.A.Rempel, Yé.V.Kuznetsova, I.B.Dorosheva, A.A.Valeeva, I.A.Weinstein, E.A.Kozlova, A.A.Saraev, D.S.Selishchev. *Top. Catal.*, **63**, 130 (2020)
70. A.B.Shishmakov, Yu.V.Mikushina, L.A.Petrov. *Russ. Chem. Bull., Int. Ed.*, **67**, 1530 (2018)
71. V.Schöllmann, J.Johansson, K.Andersen, D.V.Haviland. *J. Appl. Phys.*, **88**, 6549 (2000)
72. S.M.Barinov, V.S.Komlev. *Biokeramika na Osnove Fosfatov Kal'tsiya*. (Bioceramics Based on Calcium Phosphates). (Moscow: Nauka, 2005)
73. A.Farzin, M.Ahmadian, M.H.Fathi. *Mater. Sci. Eng.*, **33**, 2251 (2013)
74. A.A.Egorov, V.V.Smirnov, V.S.Komlev, S.M.Barinov. *Onkokhirurgiya*, **1**, 87 (2013)
75. M.Tsukada, M.Wakamura, N.Yoshida, T.Watanabe. *J. Mol. Catal. A*, **338**, 18 (2011)
76. J.Xie, X.Meng, Z.Zhou, P.Li, L.Yao, L.Bian, X.Gao, Y.Wei. *Mater. Lett.*, **110**, 57 (2013)
77. C.El Bekkali, H.Bouyarmane, S.Saoiabi, M.El Karbane, A.Rami, A.Saoiabi, M.Boujtita, A.Laghzizil. *J. Adv. Res.*, **7**, 1009 (2016)
78. C.Ergun, Z.Evis, T.J.Webster, F.C.Sahin. *Ceram. Int.*, **37**, 971 (2011)
79. S.V.Rempel, E.A.Bogdanova, A.A.Valeeva, H.Schroettner, N.A.Sabirzyanov, A.A.Rempel. *Inorg. Mater.*, **52**, 476 (2016)
80. V.P.OrLovskii, S.P.Ionov. *Zh. Neorg. Khimii*, **40**, 1961 (1995)
81. S.V.Rempel, A.A.Valeeva, E.A.Bogdanova, H.Schroettner, N.À.Sabirzyanov, A.A.Rempel. *Mendeleev Commun.*, **26**, 543 (2016)
82. S.V.Rempel, A.A.Valeeva, E.A.Bogdanova, N.A.Sabirzyanov. *Lett. Mater.*, **7**, 170 (2017)
83. S.V.Rempel, D.A.Eselevich, A.A.Valeeva, A.A.Rempel. *Inorg. Mater.*, **54**, 898 (2018)
84. S.V.Rempel, K.A.Sergeeva, H.Schroettner, A.A.Valeeva. *Nanosystems: Phys., Chem., Mathem.*, **9**, 549 (2018)
85. S.V.Rempel, D.A.Eselevich, E.Yu.Gerasimov, A.A.Valeeva. *J. Alloys Compd.*, **800**, 412 (2019)
86. A.I.Gusev, A.A.Rempel, A.J.Magerl. *Disorder and Order in Strongly Nonstoichiometric Compounds: Transition Metal Carbides, Nitrides and Oxides*. (Berlin, Heidelberg, New York, London: Springer, 2001)
87. A.I.Gusev, A.S.Kurlov. *Nanotechnology*, **19**, 265302 (2008)
88. A.S.Kurlov, A.I.Gusev. *J. Alloys Compd.*, **582**, 108 (2014)
89. A.I.Gusev. *Physics – Usp.*, **63**, 342 (2020)
90. J.Ma, M.Wu, Y.Du, S.Chen, J.Ye, L.Jin. *Mater. Lett.*, **63**, 905 (2009)
91. Z.Zhao, H.Zuo, Y.Liu, W.Song, Sh.Mao, Y.Wang. *Int. J. Refract. Met. Hard Mater.*, **27**, 971 (2009)
92. T.Taguchi, H.Yamamoto, S.Shamoto. *J. Phys. Chem. C*, **111**, 18888 (2007)
93. M.Mahajan, K.Singh, O.P.Pandey. *Int. J. Refract. Met. Hard Mate*r., **36**, 106 (2013)
94. V.N.Lipatnikov, W.Lengauer, P.Ettmayer, E.Keil, G.Groboth, E.Kny. *J. Alloys Compd.*, **261**, 192 (1997)
95. D.Rafaja, W.Lengauer, P.Ettmayer, V.N.Lipatnikov. *J. Alloys Compd.*, **269**, 60 (1998)
96. V.N.Lipatnikov, A.I.Gusev, P.Ettmayer, W.Lengauer. *J. Phys.: Condens Matter*, **11**, 163 (1999)
97. A.I.Gusev, A.S.Kurlov, A.A.Rempel. *Mendeleev Commun.*, **25**, 353 (2015)
98. A.I.Gusev, A.S.Kurlov, A.A.Rempel. *JETP Lett.*, **101**, 533 (2015)
99. A.I.Gusev, A.S.Kurlov, I.A.Bobrikov, A.M.Balagurov. *JETP Lett.*, **102**, 154 (2015)
100. A.W.Henfrey, B.E.F.Fender. *Acta Crystallogr., Sect. B*, **26**, 1882 (1970)
101. A.S.Kurlov, A.I.Gusev, E.Yu.Gerasimov, I.A.Bobrikov, A.M.Balagurov, A.A.Rempel. *Superlat. Microstruct.*, **90**, 148 (2016)
102. B.Wang, Y.Liu, J.Ye. *Phys. Scripta*, **88**, 015301 (2013)
103. A.A.Rempel, A.I.Gusev. *JETP Lett.*, **69**, 472 (1999)
104. A.M.Balagurov, I.A.Bobrikov, G.D.Bokuchava, R.N.Vasin, A.I.Gusev, A.S.Kurlov, M.Leoni. *Mater. Charact.*, **109**, 173 (2015)
105. A.I.Gusev. *Solid State Sci.*, **100**, 106092 (2020)
106. A.M.Balagurov. *Neutron News*, **16**, 8 (2005)
107. M.G.Kostenko, A.V.Lukoyanov, A.A.Valeeva. *Mendeleev Commun.*, **29**, 707 (2019)
108. A.S.Kurlov, A.I.Gusev, A.A.Rempel, V.S.Kuznetsov, I.A.Bobrikov, A.M.Balagurov. *Cryst. Res. Technol.*, **52**, 1700061 (2017)
109. V.Janickis, R.Maciuleviciuse, R.Ivanauskas, I.Ancutiene. *Colloid Polym. Sci.*, **281**, 84 (2003)
110. E.I.Yarembash, L.A.Eliseeva. *Khal'kogenidy Redkozemel'nykh Elementov*. (Rare-Earth Chalcogenides) (Moskow: Nauka, 1975)
111. R.J.Cava, F.Reidinger, B.J.Wuensch. *J. Solid State Chem.*, **31**, 69 (1980)
112. T.Blanton, S.Misture, N.Dontula, S.Zdzieszynski. *Powder Diffract.*, **26**, 110 (2011)
113. A.Tang, Y.Wang, H.Ye, C.Zhou, C.Yang, X.Li, H.Peng, F.Zhang, Y.Hou, F.Teng. *Nanotechnology*, **24**, 355602 (2013)
114. C.Cui, X.Li, J.Liu, Y.Hou, Y.Zhao, G.Zhong. *Nanoscale Res. Lett.*, **10**, 431 (2015)
115. S.I.Sadovnikov, A.I.Gusev, A.A.Rempel. *Russ. Chem. Rev.*, **85**, 731 (2016)
116. S.I.Sadovnikov, A.I.Gusev. *J. Mater. Chem. A*, **5**, 17676 (2017)
117. B.K.Patel, S.Rath, S.N.Sarangi, S.N.Sahu. *Appl. Phys. A*, **86**, 447 (2007)
118. S.Lin, Y.Feng, X.Wen, P.Zhang, S.Woo, S.Shrestha, G.Conibeer, S.Huang. *J. Phys. Chem. C*, **119**, 867 (2015)
119. N.K.Reddy, M.Devika, E.S.R.Gopal. *Crit. Rev. Solid State Mater. Sci.*, **40**, 359 (2015)
120. S.I.Sadovnikov. *Russ. Chem. Rev.*, **88**, 571 (2019)
121. Y.Xie, A.Riedinger, M.Prato, A.Casu, A.Genovese, P.Guardia, S.Sottini, C.Sangregorio, K.Miszta, S.Ghosh, T.Pellegrino, L.Manna. *J. Am. Chem. Soc.*, **135**, 17630 (2013)
122. J. Zhang, L.Sun, S.Liao, C.Yan. *Solid State Commun.*, **124**, 45 (2002)
123. G.S.Wu, X.Y.Yuan, T.Xie, G.C.Xu, L.D.Zhang, Y.L.Zhuang. *Mater. Lett.*, **58**, 794 (2004)
124. A.A.Rempel, A.Magerl. *Acta Crystallogr.*, **66**, 479 (2010)
125. A.S.Vorokh, A.A.Rempel. *JETP Lett.*, **91**, 100 (2010)
126. N.K.Morozova, N.D.Danilevich, V.I.Oleshko, S.S.Vil'chinskaya. *Izv. Vuzov. Elektronika*, **1**, 93 (2012)
127. M.A.Hines, P.Guyot-Sionnest. *J. Phys. Chem.*, **100**, 468 (1996)

128. N.Jumaa, M.Lansalot, A.Thtrets, A.Elaissari, A.Sukhanova, M.Artemyev, I.Nabiev, J.N.M.Cohen. *Langmuir*, **22**, 1810 (2006)
129. S.V.Rempel, N.S.Kozhevnikova, N.N.Aleksandrova, A.A.Rempel. *Inorg. Mater.*, **47**, 223 (2011)
130. A.I.Ekimov, I.A.Kudryavtsev, M.G.Ivanov, A.L.Efros. *Sov. Phys. Solid State*, **31**, 1385 (1989)
131. H.Okamoto, J.Matsuoka, H.Nasu, K.Kamiya. *J. Appl. Phys.*, **75**, 2251 (1994)
132. B.A.Harruff, C.E.Bunker. *Langmuir*, **19**, 893 (2003)
133. S.V.Rempel, A.A.Razvodov, M.S.Nebogatikov, E.V.Shishkina, V.Ya.Shur, A.A.Rempel. *Phys. Solid State*, **55**, 624 (2013)
134. Y.Yang, H.Chen, X.Bao. *J. Cryst. Growth*, **252**, 251 (2003)
135. S.V.Rempel, A.A.Podkorytova, A.A.Rempel. *Phys. Solid State*, **56**, 568 (2014)
136. I.D.Popov, Yé.V.Kuznetsova, S.V.Rempel, A.A.Rempel. *J. Nanopart. Res.*, **20**, 78 (2018)
137. X.S.Zxao, J.Schroeder, P.D.Persant, T.G.Bilodeau. *Phys. Rev. B*, **43**, 12580. (1991)
138. S.V.Rempel, Yu.V.Kuznetsova, I.D.Popov, A.A.Rempel. *J. Alloys Compd.*, **823**, 153811 (2020)
139. I.D.Popov, B.Sochor, B.Schummer, Yu.V.Kuznetsova, S.V.Rempel, S.Gerth, A.A.Rempel. *J. Non-Cryst. Solids*, **529**, 119781 (2020)
140. S.Seghaier, N.Camoun, R.Brini, A.B.Amara. *Mater. Chem. Phys.*, **97**, 71 (2006)
141. S.B.Qadri, A.Singh, M.Yousuf. *Thin Solid Films*, **431** – **432**, 506 (2003)
142. F.A.Fernandez-Lima, Y.Gonzalez-Alfaro, E.M.Larramendi, H.D.Fonseca Filho, M.E.H.Maia da Costa, F.L.Freire Jr, R.Prioli, R.R.de Avillez, E.F.da Silveira, O.Calzadilla, O.de Melo, E.Pedrero, E.Hernández. *Mater. Sci. Eng. B*, **136**, 187 (2007)
143. S.I.Sadovnikov, A.I.Gusev, A.A.Rempel. *JETP Lett.*, **89**, 238 (2009)
144. S.I.Sadovnikov, A.A.Rempel. *Phys. Solid State*, **51**, 2375 (2009)
145. S.I.Sadovnikov, A.I.Gusev. *J. Alloys Compd.*, **573**, 65 (2013)
146. C.Puscher. *Dingl. Polytechn. J.*, **190**, 421 (1869)
147. K.L.Chopra, R.C.Kainthla, D.K.Pandya, A.P.Thakoor. In *Physics of Thin Films*. Vol. 12. (Eds G.Hass, M.H.Francombe, J.L.Vossen). (New York, London: Academic. Press, 1982). P. 167
148. D.Lincot, G.Hodes. In *Chemical Solution Deposition of Semiconducting and Non-metallic Films. Proceedings of the International Symposium*. (Eds D.Lincot, G.Hodes). (Pennington: The Electrochemical Society, 2006). P. 1
149. B.Kim, C.-S.Park, M.Murayama, M.F.Hochella. *Environ. Sci. Technol.*, **44**, 7509 (2010)
150. L.Han, Y.Lv, A.M.Asiri, A.O.Al-Youbi, B.Tu, D.Y.Zhao. *J. Mater. Chem.*, **22**, 7274 (2012)
151. S.I.Sadovnikov, A.I.Gusev, A.A.Rempel. *Phys. Chem. Chem. Phys.*, **17**, 12466 (2015)
152. S.I.Sadovnikov, A.I.Gusev, A.A.Rempel. *Dokl. Phys. Chem.*, **464**, 238 (2015)
153. S.I.Sadovnikov, A.I.Gusev, A.A.Rempel. *Superlat. Microstruct.*, **83**, 35 (2015)
154. S.I.Sadovnikov, A.I.Gusev, A.A.Rempel. *Phys. Chem. Chem. Phys.*, **17**, 20495 (2015)
155. S.I.Sadovnikov, A.I.Gusev, A.V.Chukin, A.A.Rempel. *Phys. Chem. Chem. Phys.*, **18**, 4617 (2016)
156. A.I.Gusev, S.I.Sadovnikov, A.V.Chukin, A.A.Rempel. *Phys. Solid State*, **58**, 251 (2016)
157. S.I.Sadovnikov, A.A.Rempel, A.I.Gusev. *JETP Lett.*, **106**, 587 (2017)
158. G.Zhu, Z.Xu. *J. Am. Chem. Soc.*, **133**, 148 (2011)
159. K.Terabe, T.Nakayama, T.Hasegawa, M.Aono. *J. Appl. Phys.*, **91**, 10110 (2002)
160. L.Motte, J.Urban. *J. Phys. Chem. B*, **109**, 21499 (2005)
161. E.Khon, A.Mereshchenko, A.N.Tarnovsky, K.Acharya, A.Klinkova, N.N.Hewa-Kasakarage, I.Nemitz, M.Zamkov. *Nano Lett.*, **11**, 1792 (2011)
162. J-Y.Yan, W.Zhang, S.Duan, X.-G.Zhao, A.O.Govorov. *Phys. Rev. B*, **77**, 165301 (2008)
163. A.O.Govorov, H.Zhang. *J. Phys. Chem. C*, **119**, 6181 (2015)
164. S.V.Rempel, Yu.V.Kuznetsoba, E.Yu.Gerasimov, A.A.Rempel. *Phys. Solid State*, **59**, 1629 (2017)
165. M.Yarema, S.Pichler, M.Sytnyk, R.Seyrkammer, R.T.Lechner, G.Fritz-Popovski, D.Jarzab, K.Szendrei, R.Resel, O.Korovyanko, M.A.Loi, O.Paris, G.Hesser, W.Heiss. *ACS Nano*, **5**, 3758 (2011)
166. Y.Zhang, G.Hong, Y.Zhang, G.Chen, F.Li, H.Dai, Q.Wang. *ACS Nano*, **6**, 3695 (2012)
167. C.Wang, Y.Wang, L.Xi, D.Zhang, M.Liu, X.Li, H.Sun, Q.Lin, B.Yang. *Small*, **8**, 3137 (2012)
168. G.Li, Z.Lei, Q.M.Wang. *J. Am. Chem. Soc.*, **132**, 17678 (2010)
169. E.I.Kapinus. *Russ. J. Phys. Chem.*, **85**, 668 (2011)
170. W.Yang, L.Zhang, Y.Hu, Y.Zhong, H.B.Wu, X.W.Lou. *Angew. Chem., Int. Ed.*, **51**, 11501 (2012)
171. Y.Delgado-Beleño, M.Cortez-Valadez, C.E.Martinez-Nuñez, R.Britto Hurtado, Ramón A.B.Alvarez, O.Rocha-Rocha, H.Arizpe-Chávez, A.Perez-Rodríguez, M.Flores-Acosta. *Chem. Phys.*, **463**, 106 (2015)
172. S.V.Rempel, N.N.Aleksandrova, Yu.V.Kuznetsova, E.Yu.Gerasimov. *Inorg. Mater.*, **52**, 101 (2016)
173. Y.Delgado-Beleño, C.E.Martinez-Nuñez, M.Cortez-Valadez, N.S.Flores-López, M.Flores-Acosta. *Mater. Res. Bull.*, **99**, 385 (2018)
174. W.P.Lim, Z.Zhang, H.Y.Low, W.S.Chin. *Angew. Chem., Int. Ed.*, **43**, 5685 (2004)
175. Q.Tang, S.M.Yoon, H.J.Yang, Y.Lee, H.J.Song, H.R.Byon, H.C.Choi. *Langmuir*, **22**, 2802 (2006)
176. A.C.C.Esteves, T.Trindade. *Curr. Opinion Solid State Mater. Sci.*, **6**, 347 (2002)
177. Y.Zhao, D.W.Zhang, W.F.Shi. *Mater. Lett.*, **61**, 3232 (2007)
178. M.H.Chen, L.Gao. *Mater. Lett.*, **60**, 1059 (2006)
179. Z.Zhuang, Q.Peng, X.Wang, Y.Li. *Angew. Chem., Int. Ed.*, **46**, 8174 (2007)
180. Y.Z.Sun, B.B.Zhou. *Mater. Lett.*, **64**, 1347 (2010)
181. X.Wang, J. Zhuang, Q.Peng, Y.D.Li. *Nature (London)*, **437**, 121 (2005)
182. Hocaoglu, M.N.Çizmeciyan, R.Erdem, C.Ozen, A.Kurt, A.Sennaroglu, H.Y.Acar. *J. Mater. Chem.*, **22**, 14674 (2012)
183. J.Chen, T.Zhang, L.L.Feng, M.Zhang, X.Zhang, H.Su, D.Cui. *Mater. Lett.*, **96**, 224 (2013)
184. C.Siva, C.N.Iswarya, P.Baraneedharan, M.Sivakumar. *Mater. Lett.*, **134**, 56 (2014)
185. S.J.Kim, K.S.Dae, J.Y.Park, J.Y.Lee, J.M.Yuk. *Chem. Commun.*, **53**, 11122 (2017)
186. S.I.Sadovnikov, A.I.Gusev. *Eur. J. Inorg. Chem.*, 4944 (2016)

187. S.I.Sadovnikov, A.A.Rempel, A.I.Gusev. *Russ. Chem. Rev.*, **87**, 303 (2018)
188. P.Anastas, N.Eghbali. *Chem. Soc. Rev.*, **39**, 301 (2010)
189. Yu.V.Kuznetsova, S.V.Rempel, I.D.Popov, E.Yu.Gerasimov, A.A.Rempel. *Colloids Surf. A*, **520**, 369 (2017)
190. I.A.Balyakin, Yu.V.Kuznetsova, A.A.Rempel. *Russ. J. Phys. Chem.*, **92**, 1757 (2018)
191. P.Patnaik. *Dean's Analytical Chemistry Handbook*. 2nd Edn. (New York: McGraw-Hill, 2004). Table 4.2
192. S.I.Sadovnikov, A.I.Gusev, A.A.Rempel. *Rev. Adv. Mater. Sci.*, **41**, 7 (2015)
193. S.I.Sadovnikov, Yu.V.Kuznetsova, A.A.Rempel. *Nanostruct. Nano-Object.*, **7**, 81 (2016)
194. L.-M.Lyu, M.H.Huang. *Chem. – Asian J.*, **8**, 1847 **(**2013)
195. S.I.Sadovnikov, A.I.Gusev, E.Yu.Gerasimov, A.A.Rempel. *Chem. Phys. Lett.*, **642**, 17 (2015)
196. S.I.Sadovnikov, A.I.Gusev, E.Yu.Gerasimov, A.A.Rempel. *Inorg. Mater.*, **52**, 441 (2016)
197. A.N.Belov, O.V.Pyatilova, M.I.Vorobiev. *Adv. Nanopart.*, **3**, 1 (2014)
198. S.Xiong, B.Xi, K.Zhang, Y.Chen, J.Jiang, J.Hu, H.C.Zeng. *Sci. Rep.*, **3**, 2177 (2013)
199. D.Wang, L.Liu, Y.Kim, Z.Huang, D.Pantel, D.Hesse, M.Alexe. *Appl. Phys. Lett.*, **98**, 243109 (2011)
200. H.Tanaka, T.Akai, D.Tanaka, T.Ogawa. *e-J. Surf. Sci. Nanotechnol.*, **12**, 185 (2014)
201. H.Zhang, M.Chen, D.M.Wang, L.Xu, X.D.Liu. *Opt. Mater. Express*, **6**, 2573 (2016)
202. A.I.Gusev, S.I.Sadovnikov. *Semiconductors*, **50**, 682 (2016)
203. S.I.Sadovnikov, A.I.Gusev. *J. Nanopart. Res.*, **18**, 277 (2016)
204. S.I.Sadovnikov, A.I.Gusev. *Biointerface Res. Appl. Chem.*, **6**, 1797 (2016)
205. A.I.Gusev, S.I.Sadovnikov. *Mater. Lett.*, **188**, 351 (2017)
206. S.V.Rempel, Yu.V.Kuznetsova, A.A.Rempel. *Mendeleev Commun.*, **28**, 96 (2018)
207. S.Kim, T-H.Kim, H.Kim, B-G.Park. *Appl. Phys. Lett.* **117**, 202106 (2020)
208. J.Liu, O.Auciello, E.Obaldia, B.Da, Y. Koide. *Carbon*, **172**, 112 (2021)
209. S.V.Rempel, A.A.Rempel, A.A.Valeeva. *ACS Omega*, **5**, 22513 (2020)
210. G.Gecim, S.Dönmez, E.Erkoc. *Ceram. Int.*, **47**, 1917 (2021)
211. N.Vargas-Becerril, D.A.Sánchez-Téllez, L.Zarazúa-Villalobos, D.M.González-García, M.A.Álvarez-Pérez, C.deLeón-Escobedo, L.Téllez-Jurado. *Ceram. Int.*, **46**, 28806 (2020)
212. S.-J.Seo, Y.-G.Kim. *J. Appl. Biomater. Funct. Mater.*, **18**, 1 (2020)
213. S.Mondal, G.Hoang, P.Manivasagan, H.Kim, J.Oh. *Ceram. Int.*, **45**, 17081 (2020)
214. X.Cao, G.Wang, Y.Yang, Y.Cao, X.Cao. *J. Mater. Sci.*, **56**, 7034 (2021)
215. M.Ferri, S.Campisi, M.Scavini, C.Evangelisti, P.Carniti, A.Gervasini. *Appl. Surface Sci.*, **475**, 397 (2019)
216. K.Alorku, M.Manoj, A.Yuan. *RSC Adv.*, **10**, 40923 (2020)
217. A.Jaafar, C.Hecker, P.Árki, Y.Joseph. *Bioengineering*, **7**, 127 (2020)
218. S.M.Londoño-Restrepo, M.Herrera-Lara, L.R.Bernal-Alvarez, E.M.Rivera-Muñoza, M.E.Rodriguez-García. *Ceram. Int.*, **46**, 24454 (2020)
219. M.Epple, K.Ganesan, R.Heumann, J.Klesing, A.Kovtun, S.Neumannb, V.Sokolova. *J. Mater. Chem.*, **20**, 18 (2010)
220. V.K.Bommala, M.G.Krishna, C.T.Rao. *J. Magnes. Alloys*, **7**, 72 (2019)
221. M.Hidouri, S.V.Dorozhkin, N.Albeladi. *J. Inorg. Organomet. Polym. Mater.*, **29**, 87 (2019)
222. K.Li, Y.Xue, T.Yan, L.Zhang, Y.Han. *Bioact. Materi.*, **5**, 116 (2020)
223. S.V.Rempel, D.À.Eselevich, H.Schroettner, A.A.Valeeva, A.A.Rempel. *Ceram. Int.*, **47**, 9613 (2021)
224. I.A.Balyakin, S.V.Rempel, R.E.Ryltsev, A.A.Rempel. *Phys. Rev. E*, **102**, 05212 (2020)
225. S.V.Rempel, A.I.Gusev. *Phys. Chem. Chem. Phys.*, **22**, 14918 (2020)
226. M.I.Chebanenko, D.P.Danilovich, A.A.Lobinsky, V.I.Popkov, A.A.Rempel, A.A.Valeeva. *Int. J. Hydrogen Energy*, **46**, 16907 (2021); https://doi.org/10.1016/j.ijhydene.2021.01.223
227. A.S.Kurlov, V.S.Kuznetsov, I.A.Bobrikov, A.M.Balagurov, A.I.Gusev, A.A.Rempel. *JETP Lett.*, **108**, 253 (2018)
228. M.G.Kostenko, A.V.Lukoyanov, A.A.Valeeva, A.I.Gusev. *JETP*, **129**, 863 (2019)
229. A.A.Valeeva, A.I.Gusev. *Int. J. Refract. Met. Hard Mater.*, **95**, 105435 (2021)
230. E.S.Vorontsova, Yu.V.Kuznetsova, S.V.Rempel. *AIP Conf. Proc.*, **2313**, 030042 (2020)
231. S.V.Rempel, Y.V.Kuznetsova, A.A.Rempel. *ACS Omega*, 2020, **5**, 16826 (2020)
232. S.I.Sadovnikov, A.A.Rempel. *Russ. J. Appl. Chem.*, **92**, 893 (2019)
233. S.I.Sadovnikov. *Russ. J. Inorg. Chem.*, **64**, 1309 (2019)
234. S.I.Sadovnikov. *Russ. J. Inorg. Chem.*, **65**, 1630 (2020)
235. S.I.Sadovnikov, A.I.Gusev. *RSC Advances*, **10**, 40171 (2020)
236. A.I.Gusev, S.I.Sadovnikov. *JETPLett.*, **106**, 454 (2017)
237. S.I.Sadovnikov, A.I.Gusev. *J. Mater. Chem. A*, **5**, 20289 (2017)
238. S.I.Sadovnikov, E.A.Kozlova, E.Yu.Gerasimov, A.A.Rempel. *Catal. Commun.*, **100**, 178 (2017)
239. S.I.Sadovnikov, E.A.Kozlova, E.Yu.Gerasimov, A.A.Rempel, A.I.Gusev. *Int. J. Hydrogen Energy*, **42**, 25258 (2017)
240. S.I.Sadovnikov, E.G.Vovkotrub, A.A. Rempel. *Dokl. Phys. Chem.*, **480**, 80 (2018)
241. S.I.Sadovnikov, E.G.Vovkotrub. *J. Alloys Compd.*, **766**, 140 (2018)
242. S.I.Sadovnikov, E.G.Vovkotrub. *Semiconductors*, **52**, 1763 (2018)
243. A.A.Rempel, S.I.Sadovnikov, G.Klinser, W.Sprengel. *JETP Lett.*, **107**, 4 (2018)
244. S.I.Sadovnikov, N.S.Kozhevnikova, A.A.Rempel. *Inorg. Mater.*, **47**, 837 (2011)
245. S.I.Sadovnikov, A.A.Rempel, A.I.Gusev. *Mendeleev Commun.*, **27**, 589 (2017)
246. S.I.Sadovnikov, A.I.Gusev. *Phys. Solid State*, **60**, 1308 (2018)
247. S.I.Sadovnikov. *J. Alloys Compd.*, **788**, 586 (2019)
248. S.I.Sadovnikov. *Russ. J. Inorg. Chem.*, **65**, 812 (2020)
249. S.I.Sadovnikov, A.I.Gusev. *Phys. Solid State*, **59**, 1887 (2017)]
250. S.I. Sadovnikov, A.I.Gusev. *J. Therm. Anal. Calorim.*, **131**, 1155 (2018)
251. A.I.Gusev, S.I.Sadovnikov.*Thermochim. Acta*, **660**, 1 (2018)

252. S.I.Sadovnikov, N.S.Kozhevnikova, A.A.Rempel, A.Magerl. *Thin Solid Films*, **548**, 230 (2013)
253. S.I.Sadovnikov. *Int. J. Nanosci.*, **18**, 1940061 (2019)
254. S.I.Sadovnikov. *Phys. Solid State*, **60**, 2437 (2018)
255. S.I.Sadovnikov, A.I.Gusev. *Phys. Chem. Chem. Phys.*, **23**, 2914 (2021)
256. S.I.Sadovnikov, E.Yu.Gerasimov. *Nanoscale Adv.*, 1581 (2019)
257. S.I.Sadovnikov, A.I.Gusev. *JETP Lett.*, **109**, 584 (2019)
258. S.I.Sadovnikov, A.A.Rempel. *Semiconductors*, **53**, 941 (2019)
259. S.I.Sadovnikov, A.I.Gusev. *JETP*, **129**, 1005 (2019)
260. A.I.Gusev, S.I.Sadovnikov. *JETP*, **129**, 1045 (2019)